On the Time Scale of Salinity Adjustments in a Well-Mixed River-Sea System

Hugo de Groot

TWN3002-16 Bachelor Project

Supervisors: Y.M. Dijkstra EEMCS, TU Delft
B. Bera AS, TU Delft

Date: June 30, 2023

Abstract

The salinity profile in a coastal sea-river system is the result of balancing of salt transport due to mixing of the water by tides and the freshwater discharge from the river. When for example during times of drought freshwater discharge suddenly declines, the salinity in the river may increase significantly and threaten drinking water supplies and agriculture. The time it takes for the salinity to reach the new equilibrium may be considerable. Thorough understanding of the adaptation process is essential for taking appropriate prevention measures. However, much about this adjustment process is still unknown, in particular regarding the interaction between the river and the adjacent sea. In this study, a simplified linear model is developed to describe a well-mixed river and the adjacent sea where the water flows radially away from the mouth of the river. The unique assumptions, most notably a time-independent intrusion length, allow for a unique analytical approach using the method of eigenfunction expansion.

The smallest eigenvalues are found to define a time scale of the adjustment process. The eigenfunctions provide insight about how the salinity adjustment time varies within the system. The adjustment time does not only depend on the parameters that describe the new equilibrium, but also on the initial salinity. The eigenvalue time scales corresponding to the sea and to the river can then be used to determine the time scale of the coupled system. It is found that when the sea adjusts much faster than the river, the time scale of the river is leading the adjustment. When the eigenvalue time scale of the sea is similar to or larger than the eigenvalue time scale of the river, the adjustment time is significantly increased by the sea. When salinity is increasing, the sea restricts the inflow of salt in the river, while for decreasing salinity, the sea keeps transporting salt to the river by mixing which delays the adjustment.

The model is applied to analyse a sudden decrease in freshwater discharge in the Rotterdam Waterway, which is part of the Dutch Rhine-Meuse delta. Results show that the salinity response is delayed compared to freshwater discharge, indicating that the adjustment time of the river indeed plays an important role. Further research should consider a more general dispersion relation or an extra vertical dimension to better describe estuaries that are not well-mixed. Using numerical methods there are many other possibilities to extend the model. The effect of tides on the presence and dynamics of the fresh water bulge in the sea is of specific interest.

Contents

Chapter 1

Introduction

A river and a sea are two very different bodies of water. Not only the geometry and the flow of water differ between the sea and the river, but also the water itself is very different as typical sea water contains much more salt than that in a river. Where a river meets the sea, these vastly different systems interact. Hence the river becomes a little bit salty and affected by tides, while the water in the sea becomes fresher and on average flows away from the river. The wider and lower part of the river influenced by tides is called an estuary and this is where these interactions take place. Water from the upper part of an estuary is sometimes used for drinking water and agriculture. Under normal conditions this is possible because salt does not intrude that far into the estuary. However, when freshwater river discharge declines during times of drought, salt can possibly intrude much further into the estuary and threaten drinking water supplies and agriculture. The time it takes for estuarine salinity to adjust to such a decrease in freshwater discharge may be considerable. Thorough understanding of the adaptation process is essential for taking appropriate prevention measures.

The salinity profile in an estuary is the result of the balancing of many salt transport mechanisms. The river discharge transports salt to the sea, while the salinity difference and the mixing of water between the sea and the river causes transport of salt to the river. Far in the open ocean salinity is approximately constant and it decreases in the upstream direction. Salinity does not only depend on distance from the river mouth, but salinity is generally also vertically distributed as salt water is more dense than fresh water.

Most research on estuarine salinity has been done under the assumption of steady state. Even so, Banas et al. (2004) showed that in practice the salinity might be out of balance. A method to determine a time scale corresponding to an estuarine adjustments could therefore be important in justifying whether the system is in steady state or not.

C. Kranenburg (1986) was first to develop a time scale for estuarine salinity adjustments due to a change in freshwater discharge. He studied a river where the salinity at the mouth of the river is constant. The time scale is then expressed in parameters that describe the salt transport and geometry of the estuary. Others have continued the analytical development of adjustment time scales. MacCready (2007) relates the time scale of changes in intrusion length to the time it takes for a particle to flow through the river. Both Monismith (2017) and Chen (2015) have found that adjustment times do not only depend on the new estuarine parameters, but also on the initial salinity distribution. The adjustment time is asymmetric for increasing and decreasing salinity.

Though these studies give very relevant insight in the adjustment process, they do not account for the effects of the adjacent sea. The sea is modeled as a uniform salt reservoir that can instantaneously deliver or extract salt from the mouth of the river. However, because of all the fresher water that enters the sea at the mouth of the river there is a transition region until the salinity remains constant in the open sea. In the Rhine-Meuse delta, such a transition region of up to ten kilometer in radius is observed.

Hetland and Geyer (2004) have used a numerical model that does include a coastal sea in their study on adjustment times. However, they introduced an artificial mechanism "to prevent the formation of a bulge of freshwater at the estuary mouth, which could potentially choke the estuarine inflow". It therefore remains unknown what the effect of the coastal sea on the adjustment is.

This study will specifically focus on the interactions between the coupled sea-river system and

its effect on the adjustment time. It is expected that when the sea adjust slowly, the time scale of the river is affected. We will seek answer to the research question:

> *Under what conditions and to what extent does a well-mixed radial coastal sea affect the time scale of well-mixed estuarine salinity adjustments?*

The analysis is limited to well-mixed systems. That means that vertical stratification due to density differences is not considered. Furthermore the flow is considered uniform in a rectangular river. In the sea, the flow is radially distributed. The intrusion length is assumed to be constant in time. These assumptions are stricter than in previous studies. This allows for a unique analytical approach using eigenfunction expansion. Such analytical methods are preferred as they generally provide better fundamental understanding of the process. To solve the coupled sea-river system a numerical method is used.

In Chapter 2 the simplified linear one dimensional model will be developed that captures relevant estuarine properties while retaining analytical solvability. Chapter 3 focuses on both the analytical solution method (eigenfunction expansion) and numerical solution method (finite differences). In Chapter 4 results are presented. First the effect of the sea on steady state solutions is discussed. Then an eigenvalue time scale is introduced and analysed for the uncoupled sea and river. The chapter concludes with the analysis of numerical solutions of the coupled river-sea system. In Chapter 5 the model is applied to the Rhine-Meuse delta and compared with data from a sudden period of drought in 2018. The results are discussed in Chapter 6. At last, the conclusions are set out in Chapter 7.

Chapter 2

The Model

In this chapter we will first describe the physical mechanisms that transport salt through the sea-river system. Then we will set up a simplified one dimensional model capturing most relevant properties, which is further investigated in the following chapters. Finally, dimensionless parameters are introduced and the steady state solution is presented.

2.1 Salt Balance and Transport Mechanisms

As salt is neither produced nor destroyed but only moved through the system, a change in salinity in a certain volume is accompanied by transport of salt through the boundary of that volume. Mathematically:

$$\frac{d}{dt}\int_V s dx = \oint_{\partial V} T dx, \tag{2.1}$$

where s is the salinity in the considered volume V and T is the salt transport rate through the boundary of V.

Let $s(x, y, z, t)$ denote the salinity at a certain point in space and time. We can write

$$s(x, y, z, t) = s_0(x, t) + s'(x, y, z, t), \tag{2.2}$$

where $s_0(x, t)$ is the salinity averaged over depth, width and a tidal cycle at a point in the river and $s'(x, y, z, t)$ is the deviation from that average. Similarly, the flow velocity in the longitudinal direction $u(x, y, z, t)$ can be written as

$$u(x, y, z, t) = u_0(x, t) + u'(x, y, z, t), \tag{2.3}$$

where $u_0(x, t)$ is the velocity averaged over depth, width and a tidal cycle at a point in the river which is due to freshwater discharge, and $u'(x, y, z, t)$ is the deviation from that average which includes turbulent tidal eddies, for example.

Now most generally salt is transported by the flow of water, and by molecular diffusion due to concentration differences. Molecular diffusion is negligible on estuarine scale.[1] The total transport T is therefore given by:

$$T = u_0 s_0 + u_0 s' + u' s_0 + u' s'. \tag{2.4}$$

Averaging over width and depth and averaging over a tidal cycle, only two terms remain:

$$T = \underbrace{u_0 s_0}_{T_A} + \underbrace{< \overline{u' s} >}_{T_D}, \tag{2.5}$$

where $\bar{\cdot}$ denotes cross sectional averaging and $< \cdot >$ denotes tidally averaging. The salt transport due to river flow is denoted by T_A. This advective transport is given by

$$T_A = u_0 s_0, \tag{2.6}$$

[1] The diffusion coefficients for ions in water are of order 10^{-9} m^2 s^{-1}, see for example "Transport Phenomena Data Companion" by L.P.B.M. Janssen and M.M.C.G. Warmoeskerken, 2006. The order of the dispersion coefficient is typically much larger. For example in the study by Dijkstra, Schuttelaars, and W. Kranenburg (2022), the dispersion coefficient is in the range of $25 - 500$ m^2 s^{-1}.

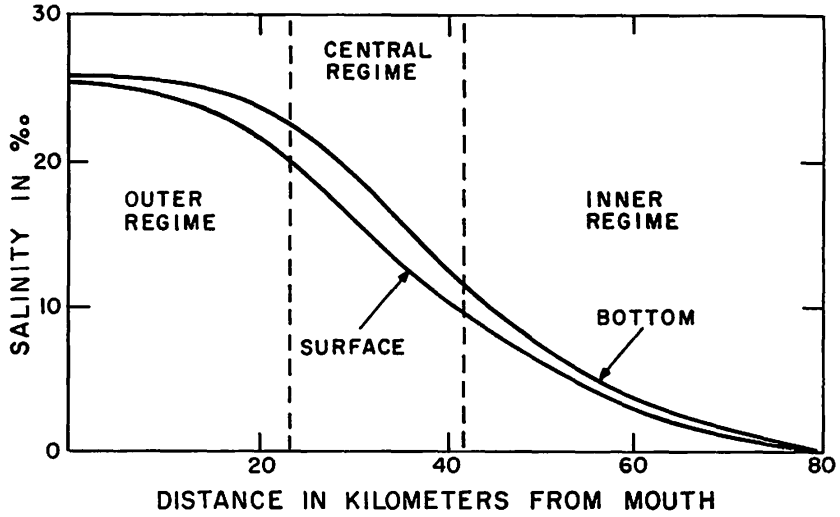

Figure 2.1: A typical salinity profile based on the Delaware River. Adopted from Figure 1 in Hansen and Rattray (1965).

where u_0 is the velocity of flow due to river discharge and equals Q/A for discharge Q through cross section A.

The flow of water u' is complicated. There is turbulent flow due to tides and gravitational circulation due to a vertical density gradient. This leads to highly nonlinear equations that can only be solved numerically. Oftentimes however, it is not practical or even necessary to consider small scale variations when analysing large systems. In this study we take the approach to simplify for the benefit of analytical solution methods. We use a dispersion relation to describe all transport that does not happen by advection due to freshwater flushing. In the simplest case, the dispersive transport T_D resembles Fickian diffusion and depends linearly on the concentration gradient by

$$T_D = -K\frac{ds_0}{dx}, \tag{2.7}$$

where K is an empirically determined parameter. Some call this eddy-diffusivity, referring to the tidal eddies that cause the transport (e.g. Chatwin (1976)), or tidal stirring.

A typical salinity profile is shown in Figure 2.1. In order the match the observed negative salinity curvature near the mouth, some let the dispersion coefficient K depend continuously on position x (e.g. MacCready (2004)). We will however generally consider the dispersion coefficient to be constant in position, and constant in time unless mentioned otherwise. The addition of the sea to the model will allow for a unique model where the dispersion is relatively simple and the typical salinity profile can be described well. Using more degrees of freedom in a nonlinear dispersion relation may provide a more accurate description at the cost of mathematical complexity.

2.2 Geometrical Setup and Partial Differential Equation

The system is divided into two separate parts as the river and sea have different characteristics, see Figure 2.2. The rectangular river is modeled with constant cross section and uniform freshwater discharge. In the sea, the freshwater discharge is assumed to be radially distributed after averaging over a tidal cycle. After defining the governing equations in the interior of the two domains, they are coupled. We will from now on denote s_0 by s for simplicity.

2.2.1 River

Let $s(x,t)$ $(\mathrm{kg\,m^{-3}})$ denote the salinity with $0 < x < L$ (m) the longitudinal position in the upstream direction of the river with $x = 0$ m at the mouth. $t > 0$ (s) is the time elapsed from a given initial salinity profile $s(x,0) = h_1(x)$, where subscript 1 emphasises the river domain. At $x = 0$ m, the salinity is considered to be a function of time $s(0,t) \equiv f(t)$, which will follow from coupling the river with the sea. At $x = L$, the salinity is 0 $\mathrm{kg\,m^{-3}}$. The water discharge Q $(\mathrm{m^3\,s^{-1}})$

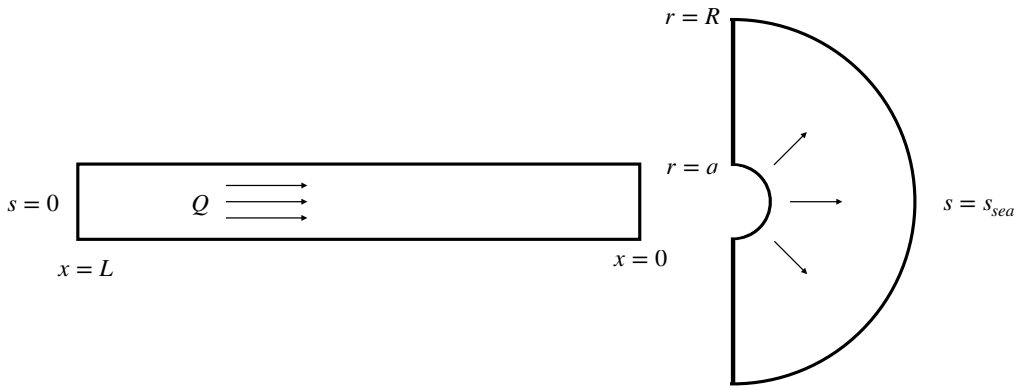

Figure 2.2: A schematic overview of the rectangular river (left) and the adjacent sea (right). The direction of flow is indicated by arrows.

flows in the negative x-direction and is taken constant in time. The cross sectional area of the river is A (m^2) is constant such that the river is rectangular. The flow velocity is $u_0 = -Q/A$. The dispersion coefficient is given as k ($\mathrm{m}^2\,\mathrm{s}^{-1}$) and is constant in time and space.

Considering the salt balance (eq. 2.1) of a small volume in the estuary with the dispersion given in equation 2.7 as demonstrated in Appendix A, results in the following partial differential equation for s:

$$\frac{\partial s}{\partial t} = k\frac{\partial^2 s}{\partial x^2} + \frac{Q}{A}\frac{\partial s}{\partial x}, \quad 0 < x < L, \quad t > 0, \tag{2.8}$$

with boundary and initial conditions

$$\begin{aligned} s(L,t) &= 0, \\ s(0,t) &= f(t), \\ s(x,0) &= h_1(x). \end{aligned} \tag{2.9}$$

2.2.2 Sea

Let $s(r,t)$ ($\mathrm{kg\,m}^{-3}$) denote the salinity with $a < r < R$ (m) the radial position in the downstream direction of the river with $r = a$ at the mouth. $t > 0$ (s) is the time elapsed from a given initial salinity profile $s(r,0) = h_2(r)$, where subscript 2 emphasises the sea domain. At $r = a$ the salinity is considered to be a function of time $s(a,t) = f(t)$, which will be determined by coupling the sea and river. At $r = R$, the salinity is a constant s_{sea}. The water discharge Q ($\mathrm{m}^3\,\mathrm{s}^{-1}$) flows in the positive r-direction and is constant in time. Note that Q is the same as in the river. The cross sectional area of the sea is $A(r) = \pi r D$, where D (m) is the depth of the sea. The dispersion coefficient is given as κ ($\mathrm{m}^2\,\mathrm{s}^{-1}$).

Again following the approach in Appendix A, we arrive at the following partial differential equation for s:

$$\frac{\partial s}{\partial t} = \kappa\frac{\partial^2 s}{\partial r^2} + \frac{1}{r}\left(\kappa - \frac{Q}{\pi D}\right)\frac{\partial s}{\partial r}, \quad a < r < R, \quad t > 0, \tag{2.10}$$

with boundary and initial conditions

$$\begin{aligned} s(a,t) &= f(t), \\ s(R,t) &= s_{sea}, \\ s(r,0) &= h_2(r). \end{aligned} \tag{2.11}$$

2.2.3 Coupling

The sea and river will be coupled at the boundaries $x = 0$ and $r = a$. The value of a follows by requiring continuity of flow velocity: $\frac{Q}{A} = \frac{Q}{\pi a D}$. At the boundary we impose the following two

conditions for the salinity:

$$s(0,t) = s(a,t) \equiv f(t), \tag{2.12}$$

$$Qs(0,t) + kAs_x(0,t) = Qs(a,t) - \kappa\pi a D s_r(a,t). \tag{2.13}$$

Here condition 2.12 imposes continuity of the salinity profile, or in other words it defines $s(r=a)$ and $s(x=0)$ to be the same point. Condition 2.13 imposes that the salt transport through this boundary layer is the same from both sides and simplified to $ks_x(0,t) = -\kappa s_r(a,t)$ using the first condition.

2.3 Dimensionless Parameters

The use of dimensionless parameters is a powerful tool as it allows for reducing the number of variables. In the partial differential equation 2.8 there are seven independent variables $(s, x, t, k, Q/A, L, s_{sea})$ and three units (kg, m, s). Using the Buckingham-Π theorem, we can express the equations in only $7-3=4$ dimensionless parameters. These are chosen as follows for the river:

$$\begin{aligned} \zeta &= s/s_{sea} \\ \xi &= \frac{x}{L} \\ \tau_1 &= \frac{tk}{L^2} \\ \mathrm{Pe} &= \frac{QL}{kA}. \end{aligned} \tag{2.14}$$

There are many ways to choose these dimensionless paramters. We chose to include the Péclet number Pe because it is the ratio of advective and dispersive transport rates. ζ and ξ are the normalised salinity and position. We find that the dimensionless time is obtained by dividing time by the dispersion time L^2/k.

In the sea-domain of equation 2.10, there are eight independent variables $(s, r, t, \kappa, Q/D, a, R, s_{sea})$. We can now change to five dimensionless parameters:

$$\begin{aligned} \zeta &= s/s_{sea} \\ \rho &= \frac{r-a}{R-a} \\ \tau_2 &= \frac{t\kappa}{(R-a)^2} \\ q &= \frac{a}{R-a} \\ P &= \frac{Q}{\kappa\pi D}. \end{aligned} \tag{2.15}$$

The dimensionless number P resembles a Péclet number where the velocity of flow is determined at the characteristic length. ζ and ρ are the normalised salinity and position and q is a parameter that describes the geometry of the sea.

The partial differential equations can then be written as

$$\frac{\partial\zeta}{\partial\tau_1} = \frac{\partial^2\zeta}{\partial\xi^2} + \mathrm{Pe}\frac{\partial\zeta}{\partial\xi}, \quad 0<\xi<1, \quad \tau_1>0, \tag{2.16}$$

subject to

$$\begin{aligned} \zeta(0,\tau_1) &= f(\tau_1)/s_{sea}, \\ \zeta(1,\tau_1) &= 0, \\ \zeta(\xi,0) &= h_1(\xi), \end{aligned} \tag{2.17}$$

and

$$\frac{\partial\zeta}{\partial\tau_2} = \frac{\partial^2\zeta}{\partial\rho^2} + \frac{1}{\rho+q}(1-P)\frac{\partial\zeta}{\partial\rho}, \quad 0<\rho<1, \quad \tau_2>0, \tag{2.18}$$

subject to

$$\begin{aligned} \zeta(0,\tau_2) &= f(\tau_2)/s_{sea}, \\ \zeta(1,\tau_2) &= 1, \\ \zeta(\rho,0) &= h_2(\rho). \end{aligned} \tag{2.19}$$

2.4 Steady State

In steady state, the salinity profile ζ does not change in time, i.e. $\frac{\partial \zeta}{\partial \tau} = 0$. In the case of a stable partial differential equation with constant coefficients, the solution will converge to its steady-state equilibrium as time goes to infinity. For $\frac{\partial \zeta}{\partial \tau} = 0$, we have a linear second order ordinary differential equation that can be solved. Let $\tilde{\zeta}$ denote the equilibrium solution, then

$$0 = \frac{d^2\tilde{\zeta}}{d\xi^2} + \mathrm{Pe}\frac{d\tilde{\zeta}}{d\xi}, \tag{2.20}$$

with solution

$$\tilde{\zeta}(\xi) = c_1 e^{-\mathrm{Pe}\xi} + c_2. \tag{2.21}$$

In the sea part we have

$$0 = \frac{d^2\tilde{\zeta}}{d\rho^2} + \frac{1-P}{\rho+q}\frac{d\tilde{\zeta}}{d\rho}, \tag{2.22}$$

with solution

$$\tilde{\zeta}(\rho) = c_3\left(\rho+q\right)^P + c_4. \tag{2.23}$$

Imposing the two boundary conditions ($\tilde{\zeta}(\xi=1)=0$, $\tilde{\zeta}(\rho=1)=1$) and the two coupling conditions ($\tilde{\zeta}(\xi=0)=\tilde{\zeta}(\rho=0)$, $-k\tilde{\zeta}_\xi(\xi=0)=\kappa\tilde{\zeta}_\rho(\rho=0)$) we can solve for the constants and find:

$$\tilde{\zeta}(\xi) = \frac{\kappa}{k}\frac{P}{\mathrm{Pe}}q^{P-1}\left[\frac{\kappa}{k}\frac{P}{\mathrm{Pe}}q^{P-1}\left(1-e^{-\mathrm{Pe}}\right)+(1+q)^P-q^P\right]^{-1}\left(e^{-\mathrm{Pe}\xi}-e^{-\mathrm{Pe}}\right), \tag{2.24}$$

$$\tilde{\zeta}(\rho) = \left[\frac{\kappa}{k}\frac{P}{\mathrm{Pe}}q^{P-1}\left(1-e^{-\mathrm{Pe}}\right)+(1+q)^P-q^P\right]^{-1}\left((\rho+q^P)-(1+q)^P\right)+1. \tag{2.25}$$

Chapter 3

Solution Methods

In this chapter we first take a look at analytical methods to solve the coupled partial differential equations. As we will see, these analytical methods provide insight into the adjustment process but do not yield an explicit closed form solution of the coupled equation. Hence in the second part of this chapter a numerical method is developed to approximate the solution. We return to the use of the original dimensional equation since we need both to have the same timescale to couple the equations. This could be done entirely in dimensionless parameters, but would be more tedious.

3.1 Analytical Methods

We will employ eigenfunction expansion in the sea and river domains separately assuming the known Dirichlet boundary condition at the coupling boundary. We will later use the remaining coupling condition to find an equation for this assumed salinity. The details of the method of eigenfunction expansion are discussed in Appendix B. The method is summarised here.

3.1.1 River

For the river we first write

$$s(x,t) = \psi(x,t) + \sum_{n=1}^{\infty} T_n(t)\phi_n(x), \tag{3.1}$$

where $\psi(x,t)$ is chosen to make the boundary conditions homogeneous for the remaining problem, which is solved by expanding it in eigenfunctions: $\sum_{n=1}^{\infty} T_n(t)\phi_n(x)$. These eigenfunction are analytically solved:

$$\phi_n(x) = e^{-\frac{Q}{2kA}x} \sin\left(\frac{n\pi x}{L}\right), \quad n \geq 1, \tag{3.2}$$

with eigenvalues

$$\lambda_n = \frac{(Q/A)^2}{4k} + k\left(\frac{n\pi}{L}\right)^2, \quad n \geq 1. \tag{3.3}$$

Note that these eigenfunctions are not orthogonal. An expression for $T_n(t)$ is derived using a Galerkin method for the first N eigenfunctions. We finally arrive at

$$\begin{aligned} T_n(t) =& e^{-\lambda_n t} \sum_{j=1}^{N} \left[G^{-1}\right]_{n,j} \int_0^L h(x)\phi_j(x)dx \\ &- f(t) \sum_{j=1}^{N} \left[G^{-1}\right]_{n,j} \int_0^L \left(1 - \frac{x}{L}\right)\phi_j(x)dx \\ &+ \int_0^t f(\bar{t}) e^{\lambda_n(\bar{t}-t)} d\bar{t} \left(\lambda_n \sum_{j=1}^{N} \left[G^{-1}\right]_{n,j} \int_0^L \left(1 - \frac{x}{L}\right)\phi_j(x)dx - \sum_{j=1}^{N} \left[G^{-1}\right]_{n,j} \int_0^L \frac{Q}{AL}\phi_j(x)dx \right). \end{aligned} \tag{3.4}$$

Here $\left[G^{-1}\right]_{n,j}$ are known coefficients from integrating products of eigenfunctions. $f(t)$ represents the unknown salinity at the boundary of the river and sea.

3.1.2 Sea

In the sea domain the same approach is applied. Only now the eigenvalues cannot be solved analytically, so a numerical root finder is used. The eigenfunctions are of the form

$$\phi_n(r) = (r)^{\frac{Q}{2\kappa\pi D}} J_{\frac{Q}{2\kappa\pi D}}\left(\sqrt{\frac{\lambda_n}{\kappa}}r\right) + d_n\,(r)^{\frac{Q}{2\kappa\pi D}} Y_{\frac{Q}{2\kappa\pi D}}\left(\sqrt{\frac{\lambda_n}{\kappa}}r\right). \tag{3.5}$$

Here J and Y are Bessel functions of the first and second kind. Following the same procedure yields

$$\begin{aligned}
T_n(t) =& e^{-\lambda_n t}\Bigg(\sum_{j=1}^{N}\left[G^{-1}\right]_{n,j}\int_a^R h(r)\phi_j(r)dr - \sum_{j=1}^{N}\left[G^{-1}\right]_{n,j}\int_a^R \frac{r-a}{R-a}\phi_j(r)dr \\
&- \frac{1}{\lambda_n}\sum_{j=1}^{N}\left[G^{-1}\right]_{n,j}\int_a^R \frac{1}{r}\left(\kappa - \frac{Q}{\pi D}\right)\frac{1}{R-a}\phi_j(r)dr\Bigg) \\
&- f(t)\sum_{j=1}^{N}\left[G^{-1}\right]_{n,j}\int_a^R \frac{R-r}{R-a}\phi_j(r)dr \\
&+ \int_0^t f(\bar{t})e^{\lambda_n(\bar{t}-t)}d\bar{t}\left(-\sum_{j=1}^{N}\left[G^{-1}\right]_{n,j}\int_a^R \frac{1}{r}\left(\kappa - \frac{Q}{\pi D}\right)\frac{1}{R-a}\phi_j(r)dr + \lambda_n\sum_{j=1}^{N}\left[G^{-1}\right]_{n,j}\int_a^R \frac{R-r}{R-a}\phi_j(r)dr\right) \\
&+ \frac{1}{\lambda_n}\sum_{j=1}^{N}\left[G^{-1}\right]_{n,j}\int_a^R \frac{1}{r}\left(\kappa - \frac{Q}{\pi D}\right)\frac{1}{R-a}\phi_j(r)dr.
\end{aligned} \tag{3.6}$$

Again, $f(t)$ remains unknown. All other terms can be (numerically) calculated.

3.1.3 Coupling

The first coupling condition 2.12 is already met by introducing $f(t)$. To solve for $f(t)$ we require the second coupling condition 2.13:

$$Qf(t) + ks_x(0,t) = Qf(t) - \kappa s_r(a,t), \tag{3.7}$$

such that

$$k\psi_x(0,t) + k\sum_{n=1}^{N} T_n(t)(\phi_n)_x(0) = -\kappa\psi_r(a,t) - \kappa\sum_{n=1}^{N} T_n(t)(\phi_n)_r(a). \tag{3.8}$$

Rewriting this equation results in a form

$$0 = \sum_{n=1}^{N} C_n^{(0)} + e^{-\lambda_n t}C_n^{(1)} + f(t)C_n^{(2)} + C_n^{(3)}\int_0^t f(\bar{t})e^{\lambda_n(\bar{t}-t)}\mathrm{d}\bar{t}. \tag{3.9}$$

Here $f(t)$ is the only unknown. All coefficients $C_n^{(i)}$ are known and can be expressed in definite integrals over the eigenfunctions, initial condition etc. It has been attempted without success to approximate the function $f(t)$ numerically by considering discrete time steps, integrating with the trapezoidal rule and then finding the root of equation 3.9 for the next time step. It is not clear why this method fails, but convergence of the differentiated series might pose a problem. The trapezoidal integration scheme does require fine time discretisation, but this does not seem to be the cause of the problem.

3.2 Numerical Methods

In this section, we will introduce a finite differences scheme that allows to determine the solution of the PDE up to any required accuracy as available computing power permits. We divide the x and r domains in n and m equidistant grid points respectively. First order spatial derivatives are approximated by second order forward differences and second order spatial derivatives are

approximated by central differences. Because of the coupling boundary conditions the first order derivatives can only be determined by forward differences. The salinity at the boundary of the two domains is eliminated from the scheme using the coupling conditions. Time integration is performed using the trapezoidal or *Crank-Nicolson* method. This method is chosen for its unconditional numerical stability. For a more detailed description, we refer to Appendix C.

The numerical scheme is consistent since the local truncation error vanishes as the grid becomes finer. The order of the method is $O(\Delta x^2 + \Delta r^2 + \Delta t^2)$. The scheme does not appear to converge very fast, i.e. many grid points must be considered to obtain an accurate solution which is computationally expensive. The trapezoidal integration method is unconditionally stable. That means that the time integration does not amplify errors as long as the approximated differential equation is analytically stable. Since we model a physical phenomena by a second order linear partial differential equation it is expected to be analytically stable. This can also be seen in the eigenfunction expansion where all terms converge under the assumption that the matrix G is invertible and $f(t)$ does converge. Hence we conclude that the numerical scheme is likely consistent and stable, and therefore convergent.

Chapter 4

Results

In this chapter the results are presented in three sections. The first section explores the steady-state salinity in the coupled river-sea system. The following section compares the eigenvalue time scales with time-dependent uncoupled solutions for increasing and decreasing freshwater discharge. This will help us to characterise the individual systems. The last section will explore the time scale of the coupled system.

4.1 Steady State

The geometry and dispersion coefficient in the sea have effect on the salinity steady state in the entire system. Figure 4.1 shows the salinity profile for different parameters to show how these parameters affect the profile. The default parameters are inspired by the Rotterdam Waterway, part of the Rhine-Meuse delta and are listed in Table 4.1. On the left, examples of salinity profiles are plotted for certain parameter values. The horizontal axis shows $-x$ and r to naturally display the estuary with the water flowing from left to right. In the panels on the right, the salinity at the mouth is plotted as function of κ (top panels), R (middle panels) and D (bottom panels). In the top panels, we can see that when κ is large, the salinity does not change much within the sea because there is a lot of mixing, while for lower κ the salinity at the mouth of the estuary can be very different from the salinity in open sea because there is not much mixing. The two middle panels show that the larger the radius of the sea is, the larger the salinity difference between the mouth of the river and the open sea. Compared with the effect of κ we notice that in this configuration halving or doubling the radius seems to have less impact than halving or doubling the dispersion coefficient. Finally, the two bottom panels show how the salinity profile changes with the depth of the sea. In a deep sea, the salinity does not change much because the flow velocity is relatively small compared with the dispersion coefficient. On the other hand, in a shallow sea the flow velocity may be relatively high such that there is a large salinity difference between the mouth at $r = a$ and the open ocean at $r = R$.

Table 4.1: Default parameter values for intrusion length L, river cross section A, radius of the sea R, depth of the sea D, water discharge Q and dispersion coefficients in the river k and in the sea κ inspired by the Rotterdam Waterway. See Chapter 5 for details about how these parameters are determined.

Parameter	Value
L	45 km
A	7500 m^2
R	7 km
D	20 m
Q	500 $\mathrm{m}^3\,\mathrm{s}^{-1}$
k	900 $\mathrm{m}^2\,\mathrm{s}^{-1}$
κ	180 $\mathrm{m}^2\,\mathrm{s}^{-1}$

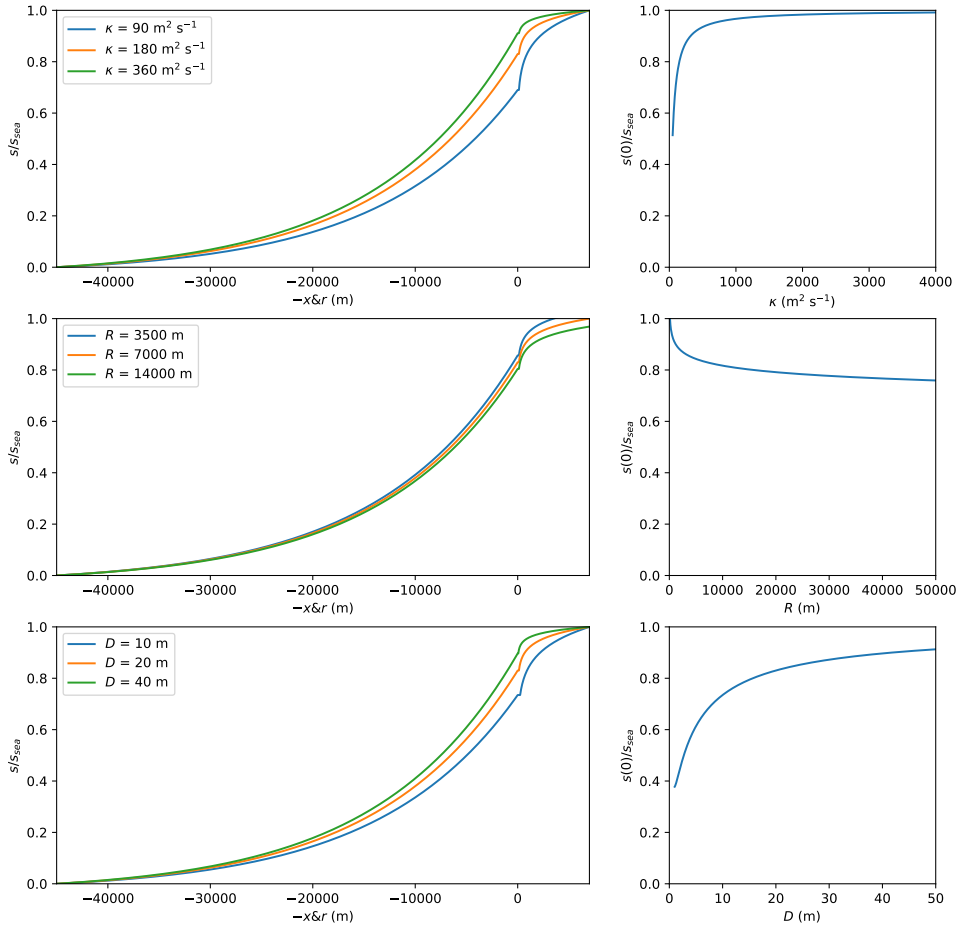

Figure 4.1: The top left panel shows the steady state salinity profile for different values sea dispersion coefficient κ. The top right panel shows the salinity at the mouth of the river as function of sea dispersion κ. The two middle panels similarly show how the size R of the transition region in the sea and the steady state solution are related. The two bottom panels show how the steady state solution and the salinity at the mouth depend on the depth of the sea D.

4.2 Eigenvalue Time Scales

Since we expect that the effect of the sea on the time scale of the adjustment process depends on the time scales of the individual sea and river subsystems, we will now investigate these separate subsystems.

We define the salinity adjustment time t_{ADJ} of the adaptation process as the time it takes to undergo $1 - 1/e$ parts ($\approx 63\%$) of the salinity adjustment, or equivalently the time at which the salinity only still needs to undergo $1/e$ of the salinity change. Mathematically we write

$$|s(x, t_{ADJ}) - s(x, \infty)| = \frac{1}{e} |s(x, 0) - s(x, \infty)| . \tag{4.1}$$

This adjustment time is a function of position (x or r). Note that the salinity increases and decreases monotonically under the used initial conditions, such that t_{ADJ} is unique for each point. To compare different estuaries and seas, we similarly define a time scale for the adjustment of total salt in the system. We write $S(t)$ for the total salt in the system. In the estuary we have $S(t) = \int_0^L As(x,t)dx$ and in the sea we have $S(t) = \int_a^R \pi r D s(r,t)dr$. The salt adjustment time T_{ADJ} is then given by

$$|S(T_{ADJ}) - S(\infty)| = \frac{1}{e} |S(0) - S(\infty)| . \tag{4.2}$$

From the eigenfunction expansion solutions 3.4 and 3.6, it is evident that the eigenvalues are important in describing the temporal behaviour of the solution. Especially the smallest eigenvalue is significant because none of the individual terms decays slower. Furthermore, the corresponding eigenmode is likely leading as the eigenfunction has no nodes and is thus expected to have the largest amplitude. It is difficult to make this statement exact as it depends on the estuarine parameters and the inverse of a matrix. Further details for an example will be discussed later in this section. Nevertheless, we argue that $1/\lambda_1$ defines a time scale of the salinity adaptation process. Then in the river, the time scale is determined by

$$\lambda_1 = \frac{(Q/A)^2}{4k} + k\frac{\pi^2}{L^2}. \tag{4.3}$$

In the sea system, we do not have an explicit expression for the eigenvalues. Since these eigenvalues are related to roots of Bessel functions, it is not expected that a polynomial or power relation is a good parameterisation. Nevertheless, a power law of the form

$$\Lambda_1 = aP^b q^c + dq^e \tag{4.4}$$

is fitted to get a better feeling for the scaling of the time scale with the parameters that describe the system. Here $\Lambda_1 = \lambda_1(R-a)^2/\kappa$ is the dimensionless smallest eigenvalue, and P and q are the dimensionless parameters as defined in section 2.3 that it depends on. This form is chosen since in the river the dimensionless eigenvalue is given by $\Lambda_1 = \frac{1}{4}\mathrm{Pe}^2 + \pi^2$ and we expect the sea may have similar behaviour with P similar to a Péclet number and with the constants possibly depending on q. If this description of Λ_1 would be the same in the sea as in the river, we would then expect $a = \frac{1}{4}, b = 2, c = 0, d = \pi^2, e = 0$. Figure 4.2 shows how Λ_1 varies for $0.001 < q < 0.1$ and $0.001 < P < 0.5$. The panel on the left shows a heat map of the eigenvalue as function of P and q. The middle panel shows the eigenvalue as function of q for some values of P and the fitted power law. The panel on the right shows the eigenvalue as function of P for some values of q and the fitted power law. The fit using an initial guess of 0 for each parameter results in the following optimal parameters $a = 0.402 \pm 0.008, b = 1.70 \pm 0.02, c = -0.340 \pm 0.003, d = 10.060 \pm 0.004, e = 0.0582 \pm 0.0001$. It should be noted that these values vary strongly for different domains. Since the chosen domain is rather large, the fit is not always accurate as can be seen in the rightmost panel of Figure 4.2. Nevertheless, it is interesting to note that the values of these parameters are similar to what we would expect based on the result in the river. We have $b = 1.70 \pm 0.02$ which is not so far from 2, as in the river. Also d and e are close to π^2 and 0.

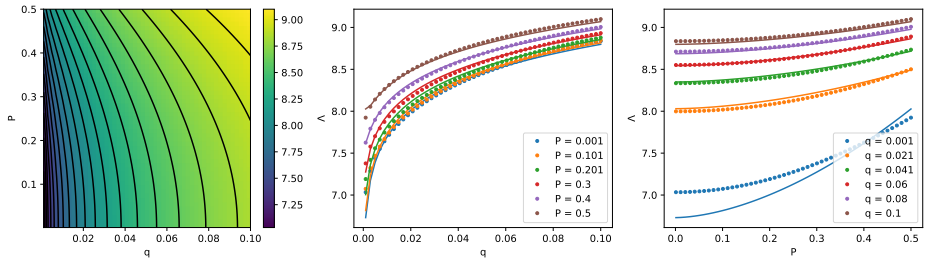

Figure 4.2: On the left a heat map of the dimensionless eigenvalue Λ_1 is shown as function of the dimensionless parameters P and q. The black lines represent constant Λ_1. In the middle and on the right, Λ_1 is plotted for constant P and q respectively. The solid lines represent a fitted power law $\Lambda_1 = (0.402 \pm 0.008)P^{1.70\pm0.02}q^{-0.340\pm0.003} + (10.060 \pm 0.004)q^{0.0582\pm0.0001}$.

4.2.1 River only

Let us now look at the adjustment time for a river only system where the boundary salinity $f(t)$ is fixed to $0.8s_{sea}$ and compare adjustment times T_{ADJ} and t_{ADJ} with $1/\lambda_1$ to check if $1/\lambda_1$ is a good time scale. To keep the results as general as possible, we will sometimes return to the dimensionless equations. The dimensionless t_{ADJ} will be denoted by τ_{ADJ}, the dimensionless T_{ADJ} will be denoted by $\mathcal{T}_{ADJ}$ and the dimensionless eigenvalue λ_1 is denoted by Λ_1. Since adjustment times may differ for increasing and decreasing salinity, we model doubling and halving of freshwater discharge by doubling and halving Péclet number Pe to the same value. Figure 4.3 shows how a typical solution evolves from the its initial condition (dashed black line) to the final steady state salinity (solid black line). At first, when the salinity is furthest away from equilibrium, the salinity adjust fastest. The time at which a point reaches the black dotted line in this figure is the adjustment time t_{ADJ}.

Figure 4.4 shows the total estuarine salt adjustment time T_{ADJ} as solid line in blue and orange for decreasing and increasing salinity. The eigenvalue time scale $1/\lambda_1$ is shown in black. Both adjustment times are smaller than $1/\lambda_1$. For decreasing salinity the adjustment time is close to $1/\lambda_1$, but for increasing salinity, the adjustment time is significantly lower.

In Figure 4.4, the local salinity adjustment time t_{ADJ} is shown as blue and orange dots for decreasing and increasing salinity. The decreasing salinity adjustment time appears relatively constant in estuarine position and close to $1/\lambda_1$. The increasing salinity adjustment time varies broadly in position. The adjustment time is much smaller near the mouth than near the intrusion length. This can be understood by the following reasoning: In the case of increasing salinity, salt must be transported upstream from the mouth of the river. Hence the salinity will first increase near the mouth, before the salt moves further up the estuary.

Even though all individual terms in the eigenfunction expansions decay faster than $1/\lambda_1$, we see that many points in the estuary have an adjustment time longer than $1/\lambda_1$. We can understand where this occurs by looking at the coefficients $T_n(t)$ of the eigenfunction expansion. Figure 4.5 shows the first ten coefficients $T_n(t)$ of the solution. In the left panel the coefficients are shown for increasing freshwater discharge. We see that the time-dependent components of $T_1(t)$ and $T_3(t)$ have the largest amplitude. Therefore, at points where $\phi_1(x)$ and $\phi_3(x)$ have the same sign, the solution decays faster than by $1/\lambda_1$. This region consists of the left- and rightmost thirds of the domain. See Appendix Figure B.1 for a plot of typical eigenfunctions. In the middle of the domain, $\phi_1(x)$ and $\phi_3(x)$ have opposing sign such that the total solution is adjusting slower than $1/\lambda_1$. This corresponds to the result in Figure 4.4. The amplitude of these time-dependent coefficients depends on the initial salinity and on the parameters that describe the new equilibrium. Thus it can be concluded that the adjustment process depends on the initial condition.

In the right panel of Figure 4.5, the first ten coefficients $T_n(t)$ are shown for decreasing freshwater discharge. We see that the time dependent component of $T_1(t)$ and $T_2(t)$ have the largest amplitude. At points where $\phi_1(x)$ and $\phi_2(x)$ have the same sign, the solution decays faster than by $1/\lambda_1$. This occurs in the half of the domain near the mouth of the river. In the other half of the domain, $\phi_1(x)$ and $\phi_2(x)$ have opposing sign such that the total solution adjusts slower than $1/\lambda_1$. Since $1/\lambda_2$ is closer to $1/\lambda_1$ than $1/\lambda_3$ is to $1/\lambda_1$, the difference in adjustment time due to the addition and subtracting of the terms is larger. This again provides an explanation for the results of Figure 4.4, where the adjustment time is generally closer to $1/\lambda_1$ for decreasing salinity.

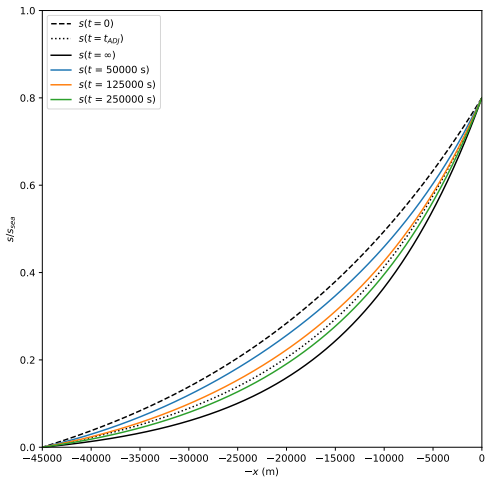

Figure 4.3: The adjusting solution due to increased discharge is shown at different times for the default parameters. The initial salinity profiles is shown as dashed black line. A point of the solution reaches the black dotted line at $t = t_{ADJ}$. As t diverges to infinity, the salinity approaches the steady state solution shown as black solid line.

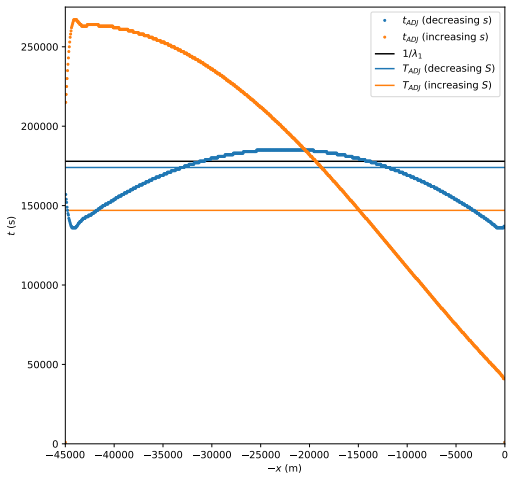

Figure 4.4: The salt adjustment time T_{adj} is shown as horizontal line for a case where water discharge is suddenly doubled in blue and halved in orange. The blue and orange dots indicate local salinity adjustment time t_{ADJ}. In black the expected time scale $1/\lambda$ is plotted. The first 50 eigenfunctions are used.

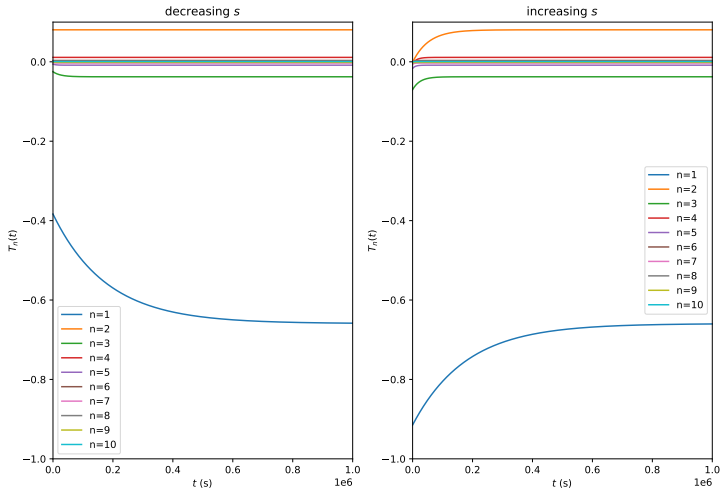

Figure 4.5: The first ten eigenfunction coefficients $T_n(t)$ are plotted for decreasing and increasing salinity due to doubling and halving of freshwater discharge in the left and right pane respectively. For decreasing salinity the time-dependent components of $T_1(t)$ and $T_3(t)$ are the largest, while for increasing salinity the time-dependent components of $T_1(t)$ and $T_2(t)$ are the largest.

To study more generally how the adjustment time T_{ADJ} and $1/\lambda_1$ are related, we return to dimensionless variables. Figure 4.6 shows how $\mathcal{T}_{ADJ}$ depends on the initial condition and Péclet number Pe. The initial condition is given by a steady state solution with $\mathrm{Pe}_0 = m\mathrm{Pe}$ (upwards pointing triangle) or $\mathrm{Pe}_0 = \frac{1}{m}\mathrm{Pe}$ (downwards pointing triangle). The width and height of the triangles are proportional to the difference between the longest and shortest local adjustment time within the estuary. This measures how evenly the adjustment time is distributed in the estuary. The color indicates the initial condition. It can be seen that adjustment times differ for different initial conditions. The adjustment time of increasing salinity is smaller than for decreasing salinity since for each Péclet number the downwards pointing triangles are above the upwards pointing triangles. The upwards pointing triangles are bigger than the downwards pointing triangles, which indicates that the local adjustment time is more evenly spread for decreasing salinity than for decreasing salinity. This corresponds to our previous result. For small Pëclet numbers, the adjustment time $\mathcal{T}_{ADJ}$ is relatively close to $1/\Lambda_1$. For larger Pëclet numbers the adjustment time becomes smaller and the deviation becomes relatively large, in particular for increasing salinity. That the adjustment time decreases for larger Pëclet numbers can be physically understood by realising that for large Péclet numbers, the salinity is initially concentrated close to the mouth of the river and the total amount of salt in the estuary is relatively small such that not much salt needs to be transported through the boundary at the mouth of the river and it does not have to be transported over a long distance.

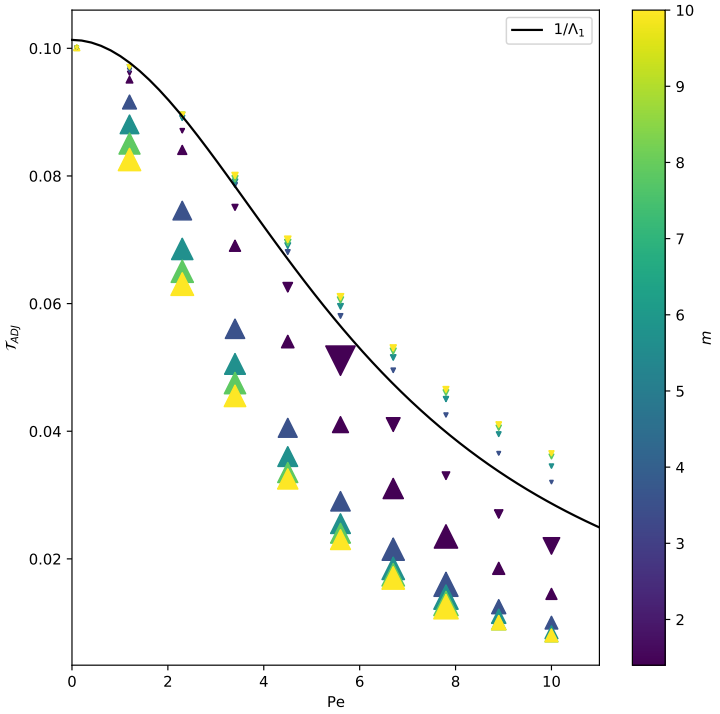

Figure 4.6: The dimensionless adjustment time $\mathcal{T}_{ADJ}$ for different Péclet numbers and different initial conditions characterised by $\mathrm{Pe}_0 = m\mathrm{Pe}$ (upwards pointing triangle) or $\mathrm{Pe}_0 = \frac{1}{m}\mathrm{Pe}$ is shown in comparison with the time scale $1/\Lambda_1$. The width and height of the triangles are proportional to the difference between longest and shortest adjustment time within the estuary. These results are obtained using the first 30 eigenfunctions.

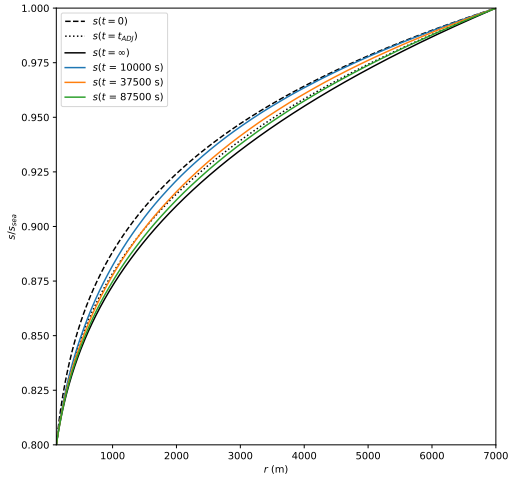

Figure 4.7: The adjusting salinity due to increased discharge for a sea with fixed boundaries is shown at different times. The solid and dashed black lines indicate the equilibrium and initial salinity. The solution locally reaches the dotted line at $t = t_{ADJ}$. The parameters are slightly adjusted for illustrative purposes.

4.2.2 Sea only

To study the smallest eigenvalue time scale in the sea, a sea only system with boundary conditions $s(a,t) = 0.8s_{sea}$ and $s(R,t) = s_{sea}$ is considered. The same procedure as for the river is followed. Figure 4.7 shows a typical solution at different times evolving from the initial condition shown as dashed black line to the final steady state equilibrium indicated by a solid black line. The time at which the solution reaches the black dotted line is the adjustment time t_{ADJ}.

Figure 4.8 shows the adjustment times corresponding to doubling and halving of P to the same value. The total salt adjustment time T_{ADJ} is shown as blue and orange solid horizontal lines for decreasing and increasing salinity respectively. They are both comparable to but slightly above the eigenvalue time scale $1/\lambda_1$ indicated by a black solid line.

The figure also shows the local salinity adjustment time t_{ADJ} indicated by blue dots for decreasing salinity and orange dots for increasing salinity. Contrary to the result in the river, the spatial variation is very similar for decreasing and increasing salinity. The adjustment time is shortest close to the mouth at $r = a$ and longest close to $r = R$, which is also different from the river system. It is believed that this is the result of the varying ratio between surface area and volume of a volume element in the sea. The solution contains more and larger oscillations than in the river only system. Increasing the number of eigenfunctions increases the accuracy but the oscillations do not disappear. Appendix D discusses the convergence of the eigenfunctions. In particular, Figure D.3 shows a similar result obtained using a numerical scheme that is very similar but does not contain these oscillations.

Figure 4.9 shows the first ten coefficients $T_n(t)$ of the eigenfunction expansion for decreasing salinity in the left pane and for increasing salinity in the right pane. We see that these coefficients are very similar for both initial conditions. Hence the observed pattern in the salinity adjustment time does also not differ much. The time varying amplitude of $T_1(t)$ and $T_2(t)$ are the largest and change in the same direction. Hence the adjustment process is faster than $1/\lambda_1$ approximately when $\phi_1(r)$ and $\phi_2(r)$ have same sign, which occurs approximately in the half of the domain close to the mouth. Analogously, the adjustment is slower than $1/\lambda_1$ approximately when $\phi_1(r)$ and $\phi_2(r)$ have opposing sign, which occurs approximately in the other half of the domain close to open sea.

Now Figure 4.10 shows the dimensionless adjustment times $\mathcal{T}_{ADJ}$ in comparison with $1/\Lambda_1$ for different values of P, only for $q = 0.02$. Values of P close to and greater than 1 are not considered since those conditions are not expected. Note that the partial differential then qualitatively changes since the term $1-P$ vanishes or becomes positive. The initial condition is the steady state solution

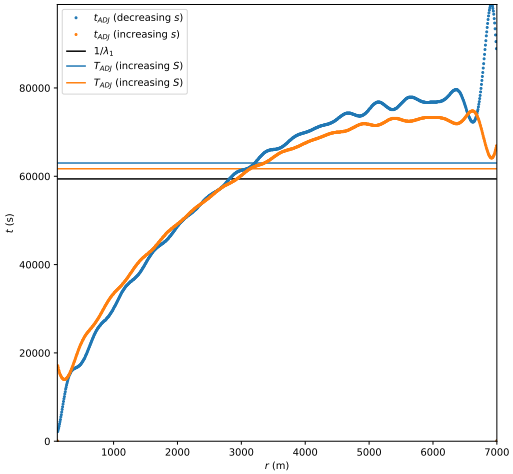

Figure 4.8: The salt adjustment time T_{ADJ} is shown as horizontal line for a case where water discharge is suddenly doubled in blue and halved in orange. The blue and orange dots indicate local salinity adjustment time t_{ADJ}. In black the eigenvalue time scale $1/\lambda_1$ is shown. The first 30 eigenfunctions are used.

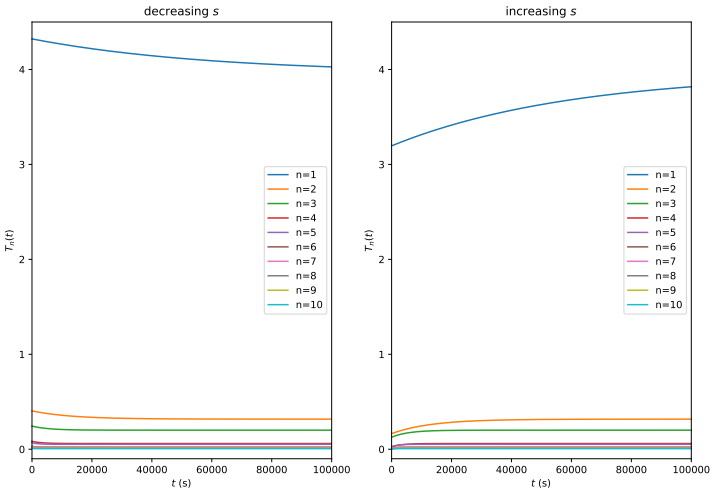

Figure 4.9: The first ten time varying coefficients $T_n(t)$ are shown for a sea with fixed boundaries. The left pane shows the result for decreasing salinity and the right pane shows the result for increasing salinity. The computation is done using the first 30 eigenmodes.

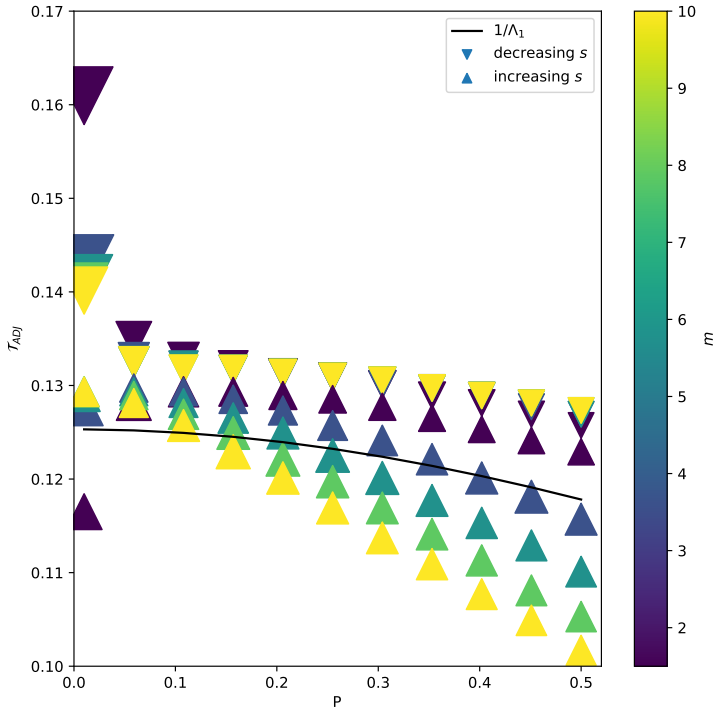

Figure 4.10: Dimensionless salt adjustment time $\mathcal{T}_{ADJ}$ is shown for different values of P with $q = 0.02$. The initial condition is the steady state solution with $P_0 = mP$ for the upwards pointing triangles and $P_0 = \frac{1}{m}P$ for downwards pointing triangles. The height and width of the triangles are proportional to the difference between the shortest and longest local adjustment time. The calculations are performed using the first 30 eigenfunctions.

with $P_0 = mP$ for the upwards pointing triangles and $P_0 = \frac{1}{m}P$ for downwards pointing triangles. The width and height of the triangles are proportional to the difference between the maximum and minimum τ_{ADJ} of that solution. For decreasing salinity we not not observe much sensitivity for the initial condition m. This is because the steady state solution is also not very sensitive for changes in P. For increasing salinity we do observe high sensitivity for m. This is because mP can become larger than 1. Then the steady state solution becomes convex instead of concave. The size of most triangles is similar, indicating a similar distribution of local adjustment times. For small P, the pattern suddenly changes and the difference between increasing and decreasing adjustment times becomes larger and for decreasing salinity the sensitivity for m increases. The increasing difference between adjustment time for increasing and decreasing salinity is confirmed using a numerical method for $m = 2$. The increase in size of the markers corresponding to a large spread in local adjustment times is likely the result of larger oscillations due to slower convergence of the eigenfunctions. For most P and m, the eigenvalue time scale gives a good indication of the adjustment time.

4.3 Time Scale of the Coupled Sea-River System

Finally, the effect of coupling the sea to the river on the time scale is investigated. Figure 4.11 shows the adjustment times t_{ADJ} (solid lines) and T_{ADJ} (dashed lines) for doubling (left pane) and halving (right pane) river discharge for varying sea dispersion κ. The eigenvalue time scale is indicated by a horizontal dotted line for both the river and the sea. This is similar to Figures 4.4 and 4.8. These results are obtained using the second order numerical model as described in Section 3.2 with 2000 grid points in the river domain and 6000 grid points in the sea domain and a time step of 1000 s. See Section D.2 for some more details about these numerical parameters.

For decreasing salinity we see that when the sea time scale is much smaller than the river time scale (purple, red), the salt adjustment time in the river and sea are very similar and close to the eigenvalue time scale of the river. Within the river, the local salinity adjustment time t_{ADJ} is distributed as in the river only system. This is to be expected since for these relatively large sea dispersion, the sea is not a limiting factor. Within the sea the salinity adjustment time is therefore also fairly constant. For some smaller sea dispersion (green, orange) where the eigenvalue time scale of the sea is still below the time scale of the river, the salt adjustment times T_{ADJ} in the river are longer than the river eigenvalue time scale, i.e. the sea slows down the adjustment in the river. Now t_{ADJ} is shortest near the intrusion length, where the sea has only little influence. Near the mouth of the river this adjustment time increases. Within the sea, the pattern of t_{ADJ} is similar to the sea only situation. The adjustment time is only much longer, because the salinity can only reach equilibrium after equilibrium has been reached upstream in the river. When the sea dispersion coefficient is even smaller (blue) and the eigenvalue time scale of the sea is above the time scale of the river, the adjustment is even slower. Because the sea adjust slowly, there will for a long time still be a large dispersive transport into the river which slows down the adjustment of the river. We conclude that the slower the salinity in the sea decreases, the slower the salinity in the river decreases. Furthermore, the slower the sea is relative to the river, the more the sea slows down the adjustment.

For increasing salinity, salt must be transported upstream from the open sea to the mouth of the river and further. When the sea dispersion coefficient is large (purple, red) and the time scale of the sea is small compared with the time scale of the river, we observe that the salt adjustment time T_{ADJ} of the river is close to the eigenvalue time scale. In the sea, the adjustment time is equal to the local adjustment time at the mouth of the river. Because of the large dispersion, the sea is mixed very fast and equally, such that the local adjustment time t_{ADJ} is almost constant within the sea. Within the river, the result is similar to the river only situation because the sea can almost instantly transport salt from the open sea to the mouth of the river. The adjustment time is longest near the intrusion length because it takes longer to transport salt further in the estuary. For somewhat smaller sea dispersion coefficients (green, orange) we observe that the adjustment time is increased because the transport of salt from the open ocean to the mouth of the river now happens less quickly. Interestingly, the salinity adjustment time t_{ADJ} is now minimal near the mouth of the river. In the river the pattern has not changed compared with the case of larger sea dispersion coefficients, but within the sea, the salinity is adjusted quicker near the mouth of the river than near the open ocean resembling the sea only situation. When the dispersion coefficient is even larger (blue) and the eigenvalue time scale of the sea is longer than the eigenvalue time scale of the river, the sea is still adjusted before the river since all salt had to be transported through the sea. The pattern of t_{ADJ} remains similar but shows a remarkable jump around the mouth of the river. This may be caused by inaccuracy of the numerical method related to the transport coupling condition for these numerical parameters given that $k = 50\kappa$. We conclude that the slower the salinity in the sea increases, the slower the salinity in the river increases because salt has to be transported through the sea. The longer the time scale of sea is relative to the river, the more the adjustment in the river is slowed down.

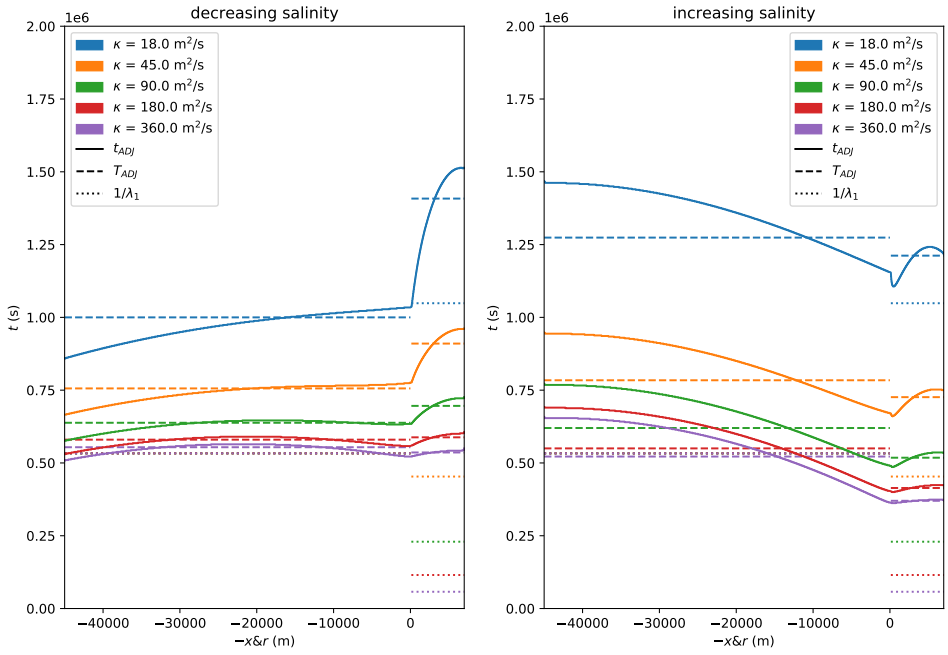

Figure 4.11: The salinity adjustment times T_{ADJ} (dashed lines) and t_{ADJ} (solid lines) are shown for different values sea dispersion κ. The left pane shows the result for decreasing salinity (increasing discharge) and the right pane for increasing salinity (decreasing discharge). Dotted lines indicate the $1/\lambda_1$ time scales in the river and in the sea.

Chapter 5

Case Study: Rotterdam Waterway

The obtained results about adjustment times is now applied to the Rotterdam Waterway, part of the Dutch Rhine-Meuse delta. Modeled results will be compared with real world data. At the Rotterdam Waterway water from both the Rhine (Switzerland, Germany, Netherlands) and the Meuse (France, Belgium, Netherlands) stream into the North Sea. In summer 2018, the freshwater discharge approximately halved in a period of approximately ten days. We will compare the salinity adjustment time with the adjustment time of the freshwater discharge, to determine if and how the adjustment time scales of the estuary and sea relate to the observed salinity adjustment time. The data we use are collected by Rijkswaterstaat.[1] They have measured water conductivity at both the Lekhaven (LEK) and the Van Brienenoordbrug (BRN) in ten minute intervals. Figure 5.1 shows these locations on a map. They are approximately 30 and 40 km upstream from the mouth of the river. We assume temperature effects are negligible and salinity is linearly proportional with conductivity such that $s/s_{sea} = \sigma/\sigma_{sea}$ where σ ($\mathrm{S\,m^{-1}}$) is the conductivity, $s_{sea} = 30$ $\mathrm{kg\,m^{-3}}$ and $\sigma_{sea} = 4$ ($\mathrm{S\,m^{-1}}$).[2]

To estimate the size of the radial sea, a model from Rijkswaterstaat is used.[3] Figure 5.2 shows the salinity in the coastal sea as determined by their model during high and low water on June 8 2023. These figures show that the transition region is the sea is indeed quite large and therefore may have an effect on the adjustment time.

Figure 5.3 shows the measured conductivity and water discharge averaged per day for the year 2018. We observe two equilibrium states. At first the water discharge and salinity are approximately constant. Then in a few days time, freshwater discharge is approximately halved. After a few more days, the salinity also appears to stabilise around a new, higher average. We will study if the salinity adjustment time is determined by the forcing time scale (freshwater discharge)

[1] Waterdata, *Rijkswaterstaat*, https://rijkswaterstaatdata.nl/waterdata/

[2] This approximation is based on Figures 1 and 5 from Tyler et al. (2017) and data from https://waterinfo.rws.nl/#!/thema/zouten/ by Rijkswaterstaat.

[3] Maasmond Viewer, *Rijkswaterstaat*, https://waterberichtgeving.rws.nl/klanten/regio-rijnmond/maasmond-viewer

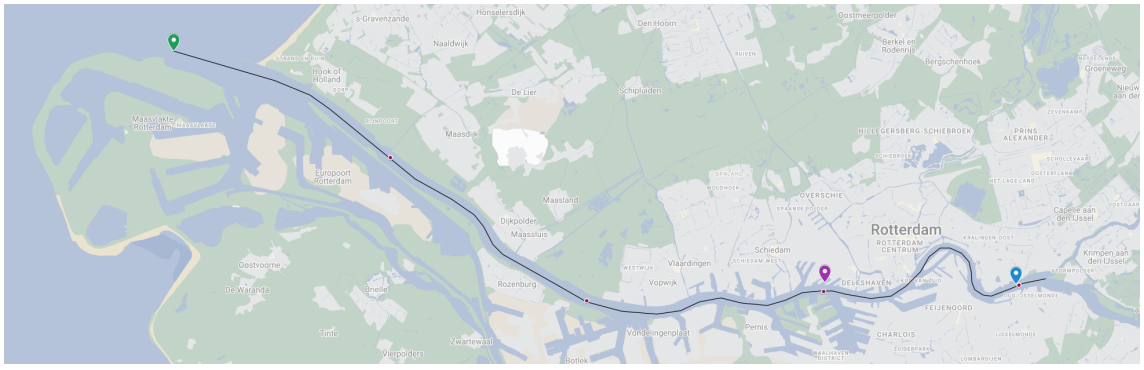

Figure 5.1: The measurement stations at the Lekhaven (purple, $x = 30$ km) and the Van Brienenoordbrug (blue, $x = 40$ km) in Rotterdam. The black line indicates the x-axis beginning at the green point where $x = 0$. 10 km intervals are indicated by dots.

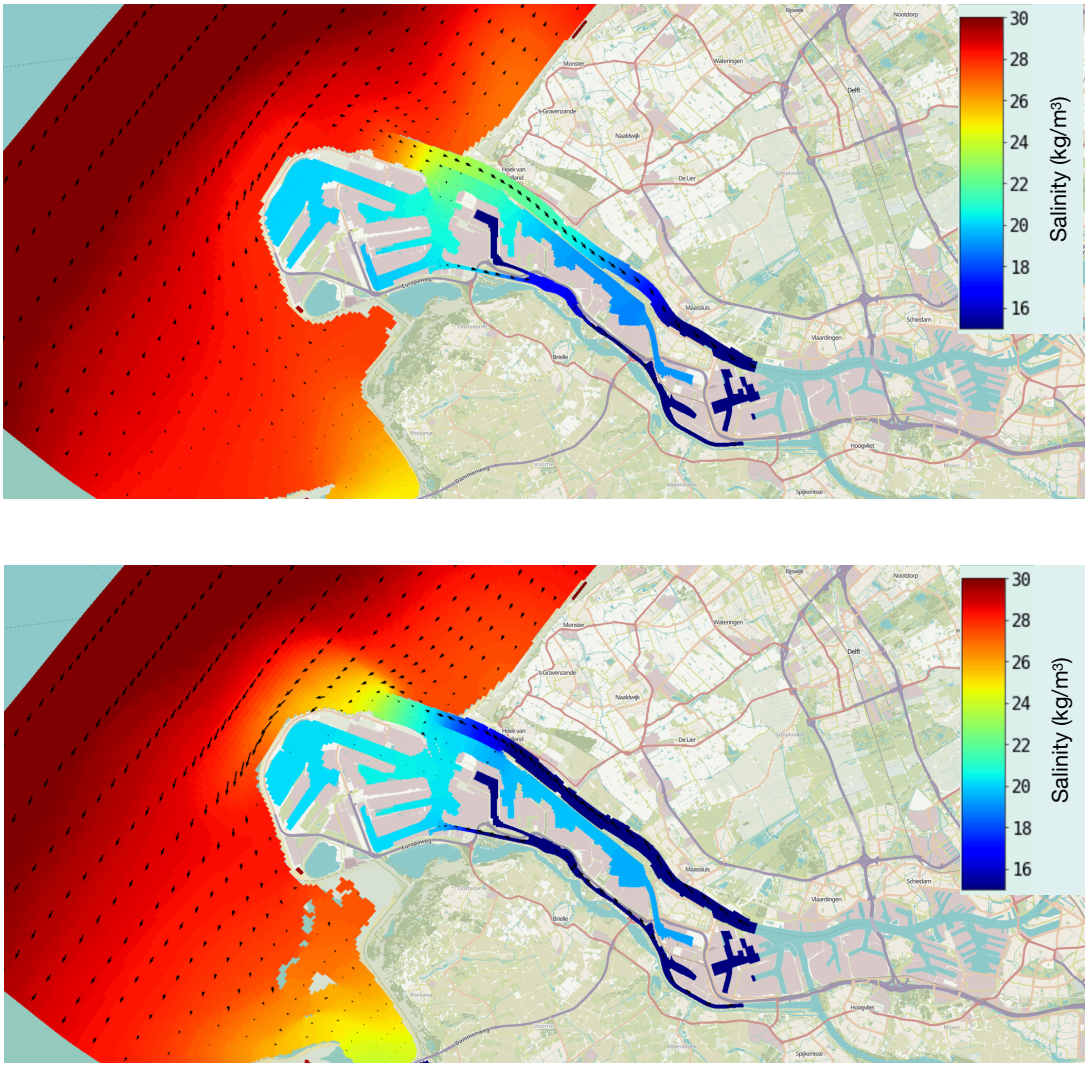

Figure 5.2: The salinity in the coastal region around the Rotterdam Waterway on June 8 is determined by Rijkswaterstaat using a complex numerical model. During both high tide (top pane) and low tide (bottom pane), there is a large transition region in the sea where salinity is not constant. During low tide the gradient in this region is larger.

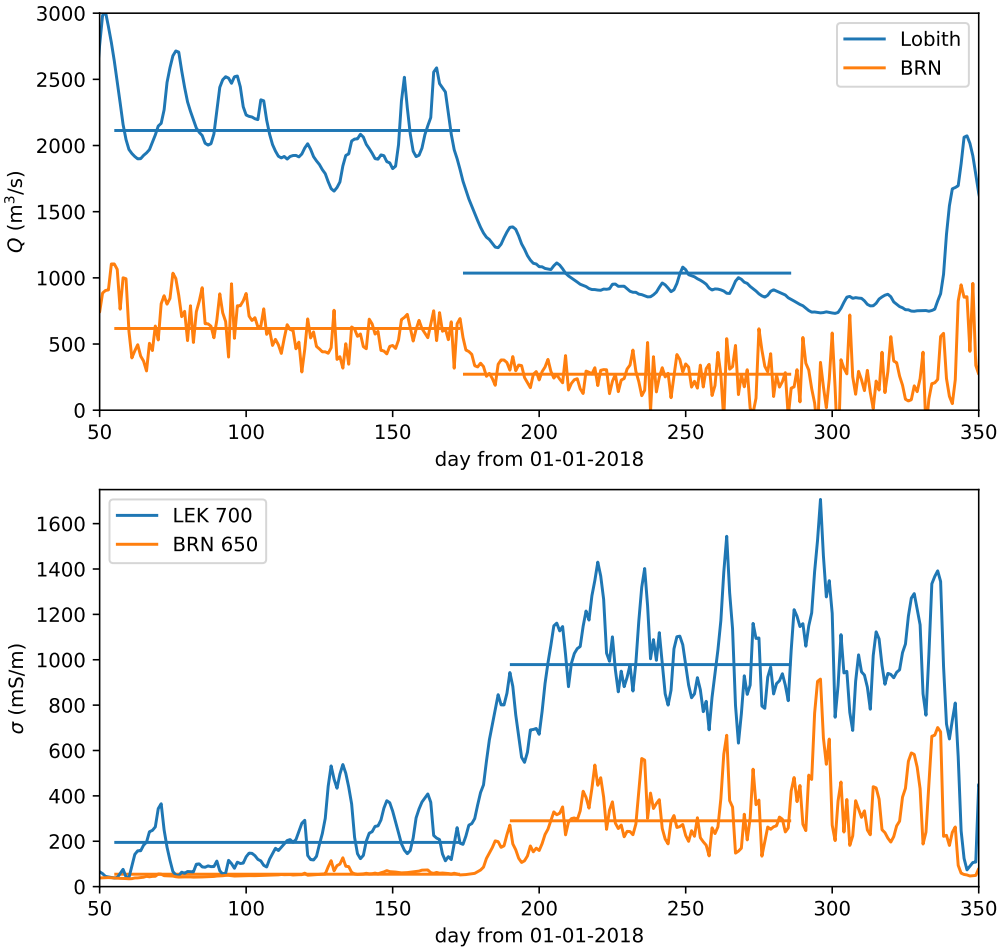

Figure 5.3: Water discharge and conductivity averaged per day at Lobith, where the Rhine enters the Netherlands, and at the Van Brienenoordbrug. Horizontal lines indicate averages over the corresponding period. Water conductivity is measured at a depth of 7.00 m at the Lekhaven and 6.50 m at the Van Brienenoordbrug.

or if the salinity is out of balance during this transition.

First we need to approximate all model parameters. R is determined from the simulation by Rijkswaterstaat in Figure 5.2 by measuring the distance between the mouth of the river and the point where the salinity reaches $s_{sea} = 30\ \mathrm{kg\,m^{-3}}$ on average during high and low tide. This is approximately 7 km. The depth of the sea is estimated to be 20 m. The cross sectional area of the river is estimated at 7500 m^2, based on a width of 500 m and depth of 15 m.[4] The salinity at $x = 0$ is estimated to be constant around 26 $\mathrm{kg\,m^{-3}}$. The dispersion coefficients and intrusion length are determined using two methods by manually fitting the steady state solution to the average salinity and flow rate before and after the change of equilibrium. The first method tries to find the best fit corresponding to the data. The other method recognises that the intrusion length must be chosen much longer to justify the approximation that there is no net transport of salt at the intrusion length. Figure 5.4 shows the fit for the parameters tabulated in Table 5.1.

[4]Width and depth are based on information from Rijkswaterstaat about the Rotterdam Waterway, see https://www.rijkswaterstaat.nl/water/vaarwegenoverzicht/nieuwe-waterweg. Upstream, the river becomes shallower and less wide, see https://www.rijkswaterstaat.nl/water/vaarwegenoverzicht/nieuwe-maas, but this is neglected.

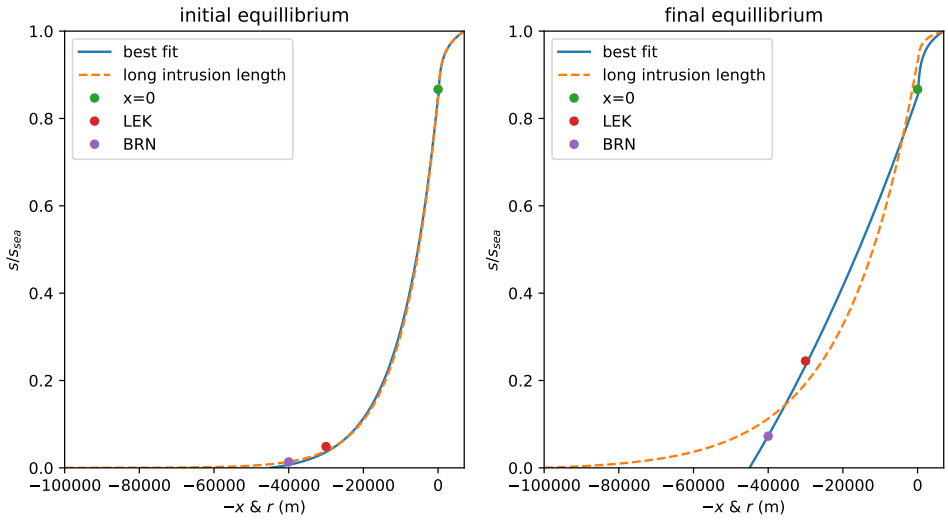

Figure 5.4: The steady state solution in the initial equilibrium state is shown on the left. On the right, the final equilibrium salinity is shown. The solution is manually fitted using two methods to the available data at the Lekhaven (LEK) and Van Brienenoordbrug (BRN).

Table 5.1: The estimated parameters for the initial and final equilibria using the method that tries to fit the data as good as possible, and a method that imposes a much longer intrusion length.

Parameter	Initial (best fit)	Final (best fit)	Initial (long intrusion)	Final (long intrusion)
L	45 km	45 km	100 km	100 km
A	7500 m^2	7500 m^2	7500 m^2	7500 m^2
R	7 km	7 km	7 km	7 km
D	20 m	20 m	20 m	20 m
Q	617 $m^3\,s^{-1}$	272 $m^3\,s^{-1}$	617 $m^3\,s^{-1}$	272 $m^3\,s^{-1}$
k	900 $m^2\,s^{-1}$	1800 $m^2\,s^{-1}$	800 $m^2\,s^{-1}$	700 $m^2\,s^{-1}$
κ	180 $m^2\,s^{-1}$	130 $m^2\,s^{-1}$	250 $m^2\,s^{-1}$	250 $m^2\,s^{-1}$

In the initial situation, the results are very similar. In the final equilibrium however the results differ significantly for a long and short intrusion length. The short intrusion length better fits the data but then there is a significant transport of salt through the upstream boundary because the gradient is large. The fact that the river is not rectangular but the cross section decreases especially after the Van Brienenoordbrug and that it consists of multiple branches, may play a role in the difference between model and observation. We will continue using both fits.

Since the river discharge does not change instantaneously but has a time scale itself, the numerical method is extended to allow for water discharge and dispersion coefficients to vary in time. This is done by recalculating the matrix K, see Appendix C, every time step. The parameters are considered to change linearly from the initial to final values as tabulated in Table 5.1. The first order method is used with 1000 spatial steps in both the sea and river with a time step of 6000 s. Running the simulation with the estimated parameters gives a result as shown in Figure 5.5. The top panel shows how water discharge changes in time, and how it is modeled using a linear and step approximation. The middle panel shows how salinity at the Lekhaven changes in time as measured and modeled. For both parameter sets, the step approximation does not model the adjustment as good as the linearly changing parameter approximation. From this we conclude that the time scale of the forcing is important. This is to be expected from the adjustment times corresponding to the parameters. With the best fit parameters we find eigenvalue time scales of 0.3 days in the sea, and 0.8 days in the river which is much faster than the time it takes for the discharge to adjust. With the long intrusion length parameters, we find eigenvalue time scales of 0.3 days in the sea, and 10 days in the river. This is of the same order as the adjustment of the water discharge. Thus the linear parameter adjustment approximation gives a result that much better resembles the shape of the measured salinity. In the calculation of the eigenvalue time scale, the order of the terms

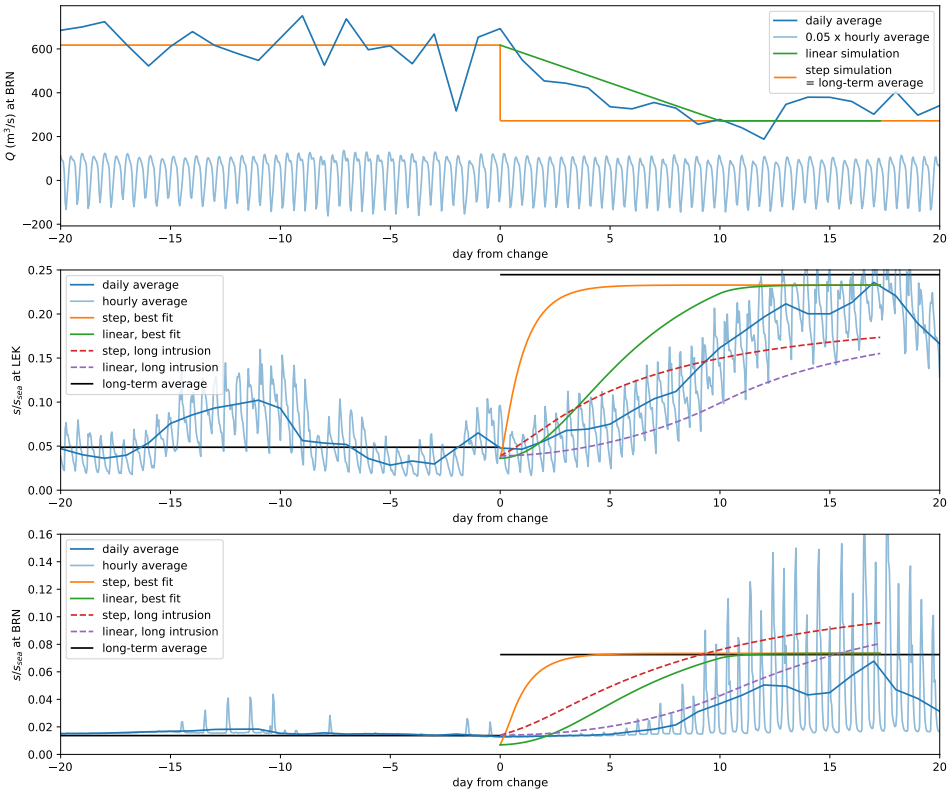

Figure 5.5: The top panels shows the measured water discharge and the approximation used in two numerical models. Salinity results at the Lekhaven and Van Brienenoordrug are shown together with the measurements in the two other panels.

$(Q/A)^2/(4k)$ and $k(\pi/L)^2$ is similar such that the eigenvalue time scale strongly correlates with the somewhat arbitrarily chosen intrusion length. The bottom panel shows the measured and modeled salinity at the van Brienenoordbrug. The result is similar to that in the Lekhaven, but now the long intrusion length approximation converges to a value above the observed salinity. Again the linearly adjusting model gives the best qualitative approximation of the adjustment process.

Chapter 6

Discussion

In steady state, the model can accurately describe a typical salinity profile as described by Hansen and Rattray (1965) despite the dispersion coefficient being constant in both the domain of the river and of the sea. This is the result of the radial flow in the sea. However, as demonstrated in the case study, the model cannot always accurately describe observed steady state salinity. The intrusion length should be large relative to dispersion (Péclet number much larger than 0) to justify the approximation that there is no net transport of salt at the intrusion length. At the intrusion length we have $s = 0$ such that there is no advective transport. Hence for there to be no net transport in steady state, there should also be no dispersive transport, corresponding to no gradient which only occurs in the limit of intrusion length to infinity. Nevertheless, we have chosen to impose a finite intrusion length, as this allows for discrete eigenvalues. This introduces a small leakage of salt at the intrusion length, which is only negligible when the intrusion length is large enough. In order to better describe salinity as observed in the Rotterdam Waterway, another dispersion relation may be better suited as Dijkstra, Schuttelaars, and W. Kranenburg (2022) show that there are different physical processes dominant in different parts of the estuary. Including gravitational circulation will make the model nonlinear, which makes the analytical method of eigenfunction expansion inapplicable. The model could also be extended to include a vertical dimension to describe the vertical distribution of salt. It would also be interesting to improve the model by letting the river cross section A be a function of x, as this might also provide a solution to make the steady-state solution better fit data in for example the Rotterdam Waterway.

The eigenvalue time scales have been shown to give a good indication of adjustment times in both a river only and sea only system with fixed boundaries for many parameter values. For increasing salinity with a large Péclet number, the eigenvalue time scale significantly overestimates the adjustment time of total salinity in the river. This is because most of the salt is concentrated near the mouth of the river. In the limit of infinite intrusion length, the scaling of $1/\lambda_1$ in the river corresponds to the time scale result by C. Kranenburg (1986) when the dispersion and geometry are chosen the same. See Appendix E for more details. In the sea, the salt adjustment time differs most from the eigenvalue time scale when P is smaller than approximately 0.01. The decreasing salt adjustment time is much less sensitive to the initial condition than the increasing salt adjustment time. We have also found that the adjustment time differs for increasing and decreasing salinity as found by for example by Hetland and Geyer (2004). It is however difficult to compare their results directly with ours, since they have increased river discharge to another value than they decrease river discharge to.

The eigenfunctions and the time-dependent coefficients in the eigenfunction expansion have provided a new method to determine how the salinity adjustment time varies within the estuary. When the salinity increases, the adjustment time is shortest near the mouth of the river, and the adjustment time is longest near intrusion length. MacCready (2007) presented a time scale related to changes in intrusion length and the result in Figure 4.4 shows an adjustment time near the intrusion length of the same order as the result by MacCready. Further investigation as presented in Appendix E shows that this similarity does not generally occur for all Péclet numbers and the results scale differently.

The presented coupled numerical solutions show how the adjacent sea affects the time scale of salinity adjustments in the estuary. This provides a simple method to estimate if the effects of the sea are significant given the parameters describing the geometry of and mixing in the sea

and the river. When the eigenvalue time scale of the sea is of similar order as or longer than the eigenvalue time scale of the river, the sea may significantly contribute to the adjustment time and must therefore not be neglected. On the other hand, if the time scale of the sea is much, say ten times, shorter than the time scale of the river, the sea could be left out of the further time scale analysis.

Further research should investigate the effect of tides on the adjustment time scale. It may be possible that the effect of a slow sea is limited when tides are strong because salt transport by a tidal flow could bypass the slowly mixing coastal sea. This would justify the approach of Hetland and Geyer (2004), who added a mechanism to their numerical model to prevent the sea from slowing down adjustment too much.

Chapter 7

Conclusion

The salinity profile in an estuary gradually adjusts when conditions change, for example in times of drought. In order to determine if, when and to what extent the adjacent coastal sea affects the time scale of this process, a model is developed and solved using a combination of numerical and analytical methods. The model consists of a rectangular river with uniform flow due to freshwater discharge and a cylindrical sea where the water flows radially away from the mouth of the river where the two systems are coupled. The system is vertically well-mixed. Next to advective transport due to river discharge, there is dispersive transport due to tidal mixing of water.

Using the method of eigenfunction expansion, a time scale determined by the smallest eigenvalue is found for the uncoupled river and sea. This time scale accurately predicts the adjustment time of total salt in these systems. Within these systems, the local salinity may adjust faster or slower depending on position. For example in case of increasing salinity, the adjustment time is longer at points further upstream because salt is imported at the mouth of the river and is only transported upstream after downstream salinity has increased. This can be understood via the eigenfunctions. It is also found that the adjustment process depends on the initial salinity distribution.

When the systems are coupled, a numerical method is used to find the solution. It is found that the addition of the sea increases the adjustment time, but the effect may be either negligible or significant depending on the relative time scales. For increasing salinity, the adjustment of the river is slowed down when the time scale of the sea is similar to or longer than the the time scale of the river. This is because the transport of salt from the open ocean to the mouth of the river happens at the time scale of the slow sea. Only when the time scale of the sea is much (i.e. ten times) shorter than the time scale of the river, the sea can transport salt fast enough from the open ocean to the river such that the adjustment time of the river is not affected much.

For decreasing salinity, similar behaviour is found. When the time scale of the sea is much shorter than the time scale of the river, the adjustment time of the river is not affected much. However when the time scale of the sea is similar to or longer than the time scale of the river, the adjustment time of the river is increased significantly because the sea keeps transporting salt to the river via mixing. The longer the time scale of the sea, the longer the adjustment time of the river.

Analysis of a sudden decrease in freshwater discharge in the Rotterdam Waterway, which is part of the Dutch Rhine-Meuse delta, shows that the time scale of the salinity response is of similar order as the eigenvalue time scale and the adjustment time of the discharge. Therefore the adjustment time of the discharge is important and it is difficult to verify if the eigenvalue time scale is accurate. The salt adjustment time is not limited by the sea, which has a much shorter time scale.

Further research should consider a more general dispersion relation or an extra vertical dimension to better describe estuaries that are not well-mixed. Using numerical methods there are many other possibilities to extend the model. The effect of tides on the presence and dynamics of the fresh water bulge in the sea is of specific interest.

Bibliography

Banas, N.S. et al. (2004). "Dynamics of Willapa Bay, Washington: A Highly Unsteady, Partially Mixed Estuary". In: *Journal of Physical Oceanography* 34(11), pp. 2413–2427. DOI: https://doi.org/10.1175/JPO2637.1.

Chatwin, P.C. (1976). "Some remarks on the maintenance of the salinity distribution in estuaries". In: *Estuarine and Coastal Marine Science* 4(5), pp. 555–566. ISSN: 0302-3524. DOI: https://doi.org/10.1016/0302-3524(76)90030-X.

Chen, S.N. (2015). "Asymmetric Estuarine Responses to Changes in River Forcing: A Consequence of Nonlinear Salt Flux". In: *Journal of Physical Oceanography* 45(11), pp. 2836–2847. DOI: https://doi.org/10.1175/JPO-D-15-0085.1.

Dijkstra, Y.M., H.M. Schuttelaars, and W.M. Kranenburg (2022). "Salt Transport Regimes Caused by Tidal and Subtidal Processes in Narrow Estuaries". In: *Journal of Geophysical Research: Oceans* 127(12), e2021JC018391. DOI: https://doi.org/10.1029/2021JC018391.

Hansen, D.V. and M. Rattray (1965). "Gravitational Circulation in Straits and Estuaries". In: *Journal of Marine Research* 23(2).

Hetland, R.D. and W.R. Geyer (2004). "An Idealized Study of the Structure of Long, Partially Mixed Estuaries". In: *Journal of Physical Oceanography* 34(12), pp. 2677–2691. DOI: https://doi.org/10.1175/JPO2646.1.

Kranenburg, C. (1986). "A Time Scale for Long-Term Salt Intrusion in Well-Mixed Estuaries". In: *Journal of Physical Oceanography* 16(7), pp. 1329–1331. DOI: https://doi.org/10.1175/1520-0485(1986)016<1329:ATSFLT>2.0.CO;2.

MacCready, P. (2004). "Toward a Unified Theory of Tidally-Averaged Estuarine Salinity Structure". In: *Estuaries* 27(4), pp. 561–570. DOI: https://doi.org/10.1007/BF02907644.

MacCready, P. (2007). "Estuarine Adjustment". In: *Journal of Physical Oceanography* 37(8), pp. 2133–2145. DOI: https://doi.org/10.1175/JPO3082.1.

Monismith, S. (2017). "An integral model of unsteady salinity intrusion in estuaries". In: *Journal of Hydraulic Research* 55(3), pp. 392–408. DOI: https://doi.org/10.1080/00221686.2016.1274682.

Tyler, R.H. et al. (2017). "Electrical Conductivity of the Global Ocean". In: *Earth, Planets and Space* 69(156). DOI: https://doi.org/10.1186/s40623-017-0739-7.

Appendix A

Deriving the PDE from the Salt Balance

River

Consider a small volume element at position x in the river with cross section A and length Δx. Then as discussed previously, averaging over width, depth and tides gives

$$\frac{d}{dt}\int_x^{x+\Delta x} As_0(\xi)d\xi = Q\left(s_0(x+\Delta x) - s_0(x)\right) + A\left(T_D(x) - T_D(x+\Delta x)\right), \tag{A.1}$$

where $Qs_0(x)$ is the advective transport rate through the boundary of the volume element, and $T_D(x)$ the dispersive transport. We now assume that $T_D(x) = -k(s_0)_x(x)$

$$\frac{d}{dt}\int_x^{x+\Delta x} As_0(\xi)d\xi = Q\left(s_0(x+\Delta x) - s_0(x)\right) + \left(-kA(s_0)_x(x) + kA(s_0)_x(x+\Delta x)\right). \tag{A.2}$$

Now using a taylor expansion around x for the integrand we obtain $s_0(\xi) = s_0(x) + (s_0)_x(x)(\xi - x) + O(\xi - x)^2$ such that

$$\begin{aligned}\frac{d}{dt}\int_x^{x+\Delta x} As_0(\xi)d\xi =& \frac{d}{dt}\int_x^{x+\Delta x} A\left(s_0(x) + (s_0)_x(x)(\xi - x) + O(\xi - x)^2\right)d\xi \\ =& \frac{\partial}{\partial t}\left[As_0(x)\xi + \frac{A}{2}(s_0)_x(x)(\xi - x)^2 + O(\xi - x)^3\right]_x^{x+\Delta x} \\ =& \frac{\partial}{\partial t}\left(As_0(x)\Delta x + O(\Delta x)^2\right).\end{aligned} \tag{A.3}$$

Substituting this into the previous equation and dividing by Δx gives

$$\frac{\partial}{\partial t}\left(As_0(x) + O(\Delta x)\right) = Q\frac{s_0(x+\Delta x) - s_0(x)}{\Delta x} + kA\frac{(s_0)_x(x+\Delta x) - (s_0)_x(x)}{\Delta x}. \tag{A.4}$$

Now taking the limit of $\Delta x \to 0$ yields

$$A\frac{\partial s_0}{\partial t} = Q\frac{\partial s_0}{\partial x} + kA\frac{\partial^2 s_0}{\partial x^2}. \tag{A.5}$$

Sea

Consider now a small volume element at position r in the sea with cross section $A(r) = \pi rD$ and length Δr. Then as discussed previously, averaging over width, depth and tides gives

$$\frac{d}{dt}\int_r^{r+\Delta r} \pi\xi Ds_0(\xi)d\xi = Q\left(s_0(r+\Delta r) - s_0(r)\right) + \left(A(r)T_D(r) - A(r+\Delta r)T_D(r+\Delta r)\right), \tag{A.6}$$

where the first part denotes advective transport, and the second braced part the dispersive transport. Assuming $T_D = -\kappa(s_0)_r(r)$ gives

$$\frac{d}{dt}\int_r^{r+\Delta r} \pi\xi D s_0(\xi) d\xi = Q\left(s_0(r+\Delta r) - s_0(r)\right) + \left(\pi D(r+\Delta r)(s_0)_r(r+\Delta r) - \pi D r (s_0)_r(r)\right). \tag{A.7}$$

Now using a taylor expansion around r for the integrand we obtain $\pi\xi D s_0(\xi) = \pi r D s_0(r) + \left(\pi D s_0(r) + \pi r D (s_0)_r(r)\right)(\xi - r) + O(\xi - r)^2$ such that

$$\begin{aligned}
\frac{d}{dt}\int_r^{r+\Delta r} A(\xi) s_0(\xi) d\xi =& \frac{d}{dt}\int_r^{r+\Delta r} \left(\pi r D s_0(r) + \left(\pi D s_0(r) + \pi r D (s_0)_r(r)\right)(\xi - r) + O(\xi - r)^2\right) d\xi \\
=& \frac{\partial}{\partial t}\left[\pi r D s_0(r)\xi + \frac{1}{2}\left(\pi D s_0(r) + \pi r D (s_0)_r(r)\right)(\xi - r)^2 + O(\xi - r)^3\right]_r^{r+\Delta r} \\
=& \frac{\partial}{\partial t}\left(\pi r \Delta r D s_0(r) + O(\Delta r)^2\right).
\end{aligned} \tag{A.8}$$

Substituting this into the previous equation and dividing by Δr gives

$$\frac{\partial}{\partial t}\left(\pi r D s_0(r) + O(\Delta r)\right) = -Q\frac{s_0(r+\Delta r) - s_0(r)}{\Delta r} + \kappa\pi D \frac{(r+\Delta r(s_0)_r(r+\Delta r) - r(s_0)_r(r)}{\Delta r}. \tag{A.9}$$

Now taking the limit of $\Delta r \to 0$ yields

$$\pi r D \frac{\partial s_0}{\partial t} = -Q\frac{\partial s_0}{\partial r} + \kappa\pi D \frac{\partial}{\partial r}\left(r\frac{\partial s_0}{\partial r}\right). \tag{A.10}$$

We finally arrive at

$$\frac{\partial s_0}{\partial t} = \kappa\frac{\partial^2 s_0}{\partial r^2} + \frac{1}{r}\left(\kappa - \frac{Q}{\pi D}\right)\frac{\partial s_0}{\partial r}. \tag{A.11}$$

Appendix B

Eigenfunction Expansion

In this chapter the details of eigenfunction expansion as introduced in chapter 3 are presented.

River

We now consider

$$s(x,t) = v(x,t) + \psi(x,t),$$

with ψ chosen such that the boundary conditions for v become homogeneous

$$\psi(x,t) = f(t)\left(1 - \frac{x}{L}\right).$$

Then the equation for v is:

$$\frac{\partial v}{\partial t} = k\frac{\partial^2 v}{\partial x^2} + \frac{Q}{A}\frac{\partial v}{\partial x} + \left[-\frac{\partial \psi}{\partial t} + k\frac{\partial^2 \psi}{\partial x^2} + \frac{Q}{A}\frac{\partial \psi}{\partial x}\right], \tag{B.1}$$

which we rewrite as

$$v_t = kv_{xx} + \frac{Q}{A}v_x + H(x,t), \tag{B.2}$$

where the Dirichlet boundary conditions for v are homogeneous and the initial condition is $v(x,0) = h(x) - \psi(x,0)$.

Related Eigenvalue Problem

The Eigenvalue Problem related to this PDE is:

$$k\phi_{xx} + \frac{Q}{A}\phi_x = -\lambda\phi. \tag{B.3}$$

It has the following solution

$$\phi_n(x) = e^{-\frac{Q}{2kA}x}\sin\left(\frac{n\pi x}{L}\right), \quad n \geq 1, \tag{B.4}$$

with

$$\lambda_n = \frac{(Q/A)^2}{4k} + k\left(\frac{n\pi}{L}\right)^2, \quad n \geq 1. \tag{B.5}$$

Figure B.1 shows the first five eigenfunctions ϕ_n and their correlation. Note that the set of eigenfunctions is not orthogonal. The greater |Pe|, the more the eigenfunctions correlate. These eigenfunctions already give some information about the solution that will be obtained. For example, when $\mathrm{Pe} \gg 1$ the amplitude of these eigenfunctions is centered close to $x = L$. There the deviation from a straight line solution (diffusion only) is greatest and salt will not intrude much into the estuary because the flow is 'strong'.

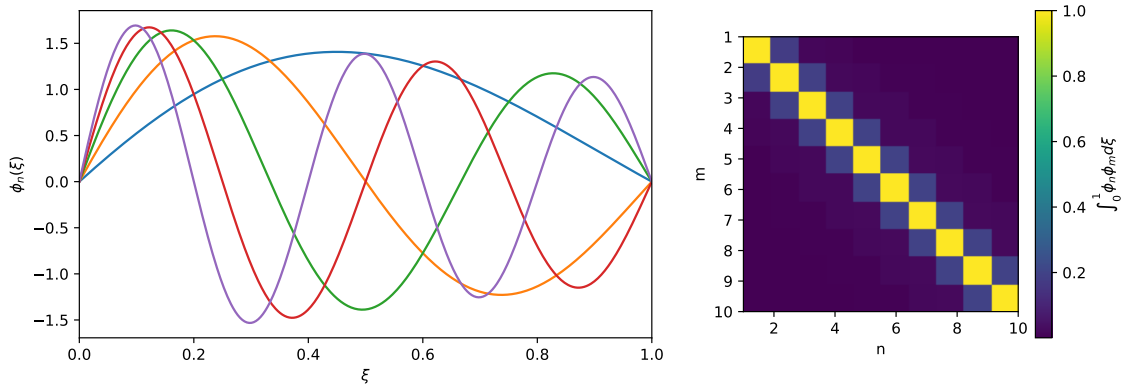

Figure B.1: The first five normalised eigenfunctions with Pe = 1 are displayed on the left. On the right the correlation is plotted.

Eigenfunction Expansion

Now that we have the eigenfunctions we can expand v into eigenfunctions:

$$v(x,t) = \sum_{n=1}^{\infty} T_n(t)\phi_n(x). \tag{B.6}$$

Substituting this into the PDE for v and using $k\phi_{xx} + \frac{Q}{A}\phi_x = -\lambda\phi$ we obtain

$$\sum_{n=1}^{\infty} \frac{dT_n(t)}{dt}\phi_n(x) = \sum_{n=1}^{\infty} -\lambda_n T_n(t)\phi_n(x) + H(x,t). \tag{B.7}$$

Multiplying by $\phi_k(x)$ for any k and integrating from 0 to L, and only considering the first N eigenmodes gives

$$\int_0^L \sum_{n=1}^{N} \frac{dT_n(t)}{dt}\phi_n(x)\phi_k(x)dx = \int_0^L \sum_{n=1}^{N} -\lambda_n T_n(t)\phi_n(x)\phi_k(x)dx + \int_0^L H(x,t)\phi_k(x)dx \tag{B.8}$$

$$\sum_{n=1}^{N} \left(\frac{dT_n(t)}{dt} + \lambda_n T_n(t)\right) \int_0^L \phi_n(x)\phi_k(x)dx = \int_0^L H(x,t)\phi_k(x)dx. \tag{B.9}$$

Or in matrix notation:

$$\underbrace{\begin{bmatrix} \int_0^L \phi_1(x)\phi_1(x)dx & \int_0^L \phi_1(x)\phi_2(x)dx & \cdots & \int_0^L \phi_1(x)\phi_N(x)dx \\ \int_0^L \phi_2(x)\phi_1(x)dx & \int_0^L \phi_2(x)\phi_2(x)dx & \cdots & \int_0^L \phi_2(x)\phi_N(x)dx \\ \vdots & \vdots & \ddots & \vdots \\ \int_0^L \phi_N(x)\phi_1(x)dx & \int_0^L \phi_N(x)\phi_2(x)dx & \cdots & \int_0^L \phi_N(x)\phi_N(x)dx \end{bmatrix}}_{G} \begin{bmatrix} \frac{dT_1(t)}{dt} + \lambda_1 T_1(t) \\ \frac{dT_2(t)}{dt} + \lambda_2 T_2(t) \\ \vdots \\ \frac{dT_N(t)}{dt} + \lambda_N T_N(t) \end{bmatrix} = \begin{bmatrix} \int_0^L H(x,t)\phi_1(x)dx \\ \int_0^L H(x,t)\phi_2(x)dx \\ \vdots \\ \int_0^L H(x,t)\phi_N(x)dx \end{bmatrix} \tag{B.10}$$

such that

$$\begin{bmatrix} \frac{dT_1(t)}{dt} + \lambda_1 T_1(t) \\ \frac{dT_2(t)}{dt} + \lambda_2 T_2(t) \\ \vdots \\ \frac{dT_N(t)}{dt} + \lambda_N T_N(t) \end{bmatrix} = G^{-1} \begin{bmatrix} \int_0^L H(x,t)\phi_1(x)dx \\ \int_0^L H(x,t)\phi_2(x)dx \\ \vdots \\ \int_0^L H(x,t)\phi_N(x)dx \end{bmatrix} \tag{B.11}$$

So we have

$$\begin{aligned}
&\frac{dT_n(t)}{dt} + \lambda_n T_n(t) = \sum_{j=1}^{N} \left[G^{-1}\right]_{n,j} \int_0^L H(x,t)\phi_j(x)dx \\
\implies & e^{\lambda_n t}\frac{dT_n(t)}{dt} + e^{\lambda_n t}\lambda_n T_n(t) = e^{\lambda_n t}\sum_{j=1}^{N} \left[G^{-1}\right]_{n,j} \int_0^L H(x,t)\phi_j(x)dx \\
\implies & \frac{d}{dt}\left[e^{\lambda_n t}T_n(t)\right] = e^{\lambda_n t}\sum_{j=1}^{N} \left[G^{-1}\right]_{n,j} \int_0^L H(x,t)\phi_j(x)dx \\
\implies & e^{\lambda_n t}T_n(t) - T_n(0) = \int_0^t e^{\lambda_n \bar{t}}\sum_{j=1}^{N} \left[G^{-1}\right]_{n,j} \int_0^L H(x,\bar{t})\phi_j(x)dx d\bar{t} \\
\implies & T_n(t) = e^{-\lambda_n t}T_n(0) + e^{-\lambda_n t}\int_0^t e^{\lambda_n \bar{t}}\sum_{j=1}^{N} \left[G^{-1}\right]_{n,j} \int_0^L H(x,\bar{t})\phi_j(x)dx d\bar{t},
\end{aligned} \tag{B.12}$$

where $T_n(0)$ is found similarly by multiplying equation B.6 at $t = 0$ by $\phi_k(x)$ and integrating from 0 to L to obtain

$$T_n(0) = \sum_{j=1}^{N} \left[G^{-1}\right]_{n,j} \int_0^L \left(h(x) - \psi(x,0)\right)\phi_j(x)dx. \tag{B.13}$$

We will now write this out as it is somewhat illustrative:

$$\begin{aligned}
T_n(t) =& e^{-\lambda_n t}\sum_{j=1}^{N} \left[G^{-1}\right]_{n,j} \int_0^L h(x)\phi_j(x)dx \\
&- f(t)\sum_{j=1}^{N} \left[G^{-1}\right]_{n,j} \int_0^L \left(1 - \frac{x}{L}\right)\phi_j(x)dx \\
&+ \int_0^t f(\bar{t})e^{\lambda_n(\bar{t}-t)}d\bar{t}\left(\lambda_n \sum_{j=1}^{N} \left[G^{-1}\right]_{n,j} \int_0^L \left(1 - \frac{x}{L}\right)\phi_j(x)dx - \sum_{j=1}^{N} \left[G^{-1}\right]_{n,j} \int_0^L \frac{Q}{AL}\phi_j(x)dx\right),
\end{aligned} \tag{B.14}$$

where we have used partial integration in this step to remove the time derivative.

Sea

We will now analogously consider the problem in the sea-domain and write

$$s(r,t) = v(r,t) + \psi(r,t), \tag{B.15}$$

with ψ (we use the same notation as previously to indicate a different function that has the same role) chosen such that the boundary conditions become homogeneous:

$$\psi(r,t) = \frac{1 - f(t)}{R - a}r + \frac{Rf(t) - a}{R - a}. \tag{B.16}$$

Then the equation for v becomes:

$$\frac{\partial v}{\partial t} = \kappa\frac{\partial^2 v}{\partial r^2} + \frac{1}{r}\left(\kappa - \frac{Q}{\pi D}\right)\frac{\partial v}{\partial r} + \left[-\frac{\partial \psi}{\partial t} + \kappa\frac{\partial^2 \psi}{\partial r^2} + \frac{1}{r}\left(\kappa - \frac{Q}{\pi D}\right)\frac{\partial \psi}{\partial r}\right], \tag{B.17}$$

which we rewrite as

$$v_t = \kappa v_{rr} + \frac{1}{r}\left(\kappa - \frac{Q}{\pi D}\right)v_r + H(r,t), \tag{B.18}$$

where the Dirichlet boundary conditions for v are homogeneous and the initial condition is $v(r,0) = h(r) - \psi(r,0)$.

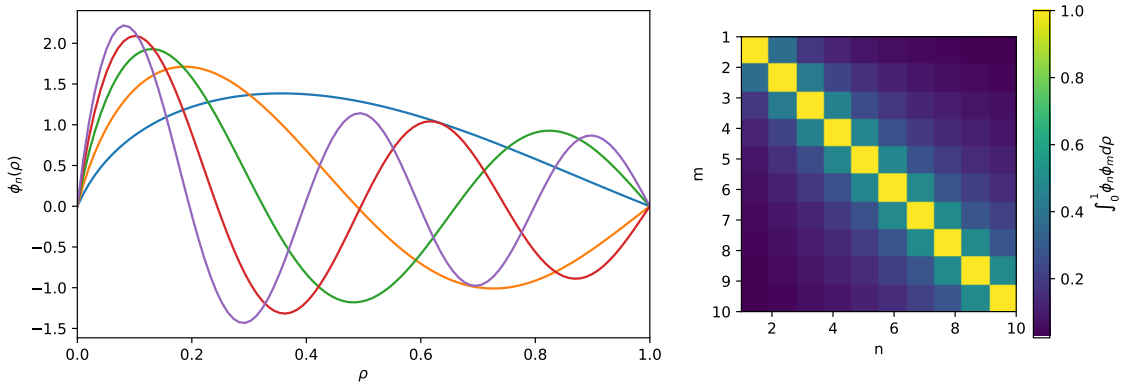

Figure B.2: The first five normalised eigenfunctions with P = 0.01, $q = 0.05$ are displayed on the left. On the right their correlation is shown.

Related Eigenvalue Problem

The Eigenvalue Problem related to this PDE is

$$\kappa\phi_{rr} + \frac{1}{r}\left(\kappa - \frac{Q}{\pi D}\right)\phi_r = -\lambda\phi. \tag{B.19}$$

This equation is a little more peculiar. One could use the method of Frobenius to find a series solution. One could also recognize the following standard form:

$$\phi_n(r) = (r)^{\frac{Q}{2\kappa\pi D}} J_{\frac{Q}{2\kappa\pi D}}\left(\sqrt{\frac{\lambda_n}{\kappa}}r\right) + d_n\,(r)^{\frac{Q}{2\kappa\pi D}} Y_{\frac{Q}{2\kappa\pi D}}\left(\sqrt{\frac{\lambda_n}{\kappa}}r\right), \tag{B.20}$$

where $J_{\frac{Q}{2\kappa\pi D}}$ and $Y_{\frac{Q}{2\kappa\pi D}}$ are Bessel functions of fractional order $\frac{Q}{2\kappa\pi D}$ of the first and second kind respectively. In order to find the eigenvalues λ_n and the constants d_n such that the homogeneous Dirichlet boundary conditions are satisfied, a numerical root finder may be used. The eigenfunctions appear to be rather well-behaving with $\lambda_1 < \lambda_2 < \cdots$ with $n-1$ zero-crossings. Figure B.2 shows the first five eigenfunctions ϕ_n. Note that the set of eigenfunctions is not orthogonal.

Eigenfunction Expansion

Now that we have the eigenfunctions we expand v in its eigenfunctions:

$$v(r,t) = \sum_{n=1}^{\infty} T_n(t)\phi_n(r). \tag{B.21}$$

Substituting this into the PDE for v and using $\kappa\phi_{rr} + \frac{1}{r}\left(\kappa - \frac{Q}{\pi D}\right)\phi_r = -\lambda\phi$ we obtain

$$\sum_{n=1}^{\infty} \frac{dT_n(t)}{dt}\phi_n(r) = \sum_{n=1}^{\infty} -\lambda_n T_n(t)\phi_n(r) + H(r,t). \tag{B.22}$$

Multiplying by $\phi_k(r)$ and integrating from a to R, and only considering the first N eigenmodes gives

$$\int_a^R \sum_{n=1}^{N} \frac{dT_n(t)}{dt}\phi_n(r)\phi_k(r)dr = \int_a^R \sum_{n=1}^{N} -\lambda_n T_n(t)\phi_n(r)\phi_k(r)dr + \int_0 a^R H(r,t)\phi_k(r)dr, \tag{B.23}$$

$$\sum_{n=1}^{N}\left(\frac{dT_n(t)}{dt} + \lambda_n T_n(t)\right)\int_a^R \phi_n(r)\phi_k(r)dr = \int_a^R H(r,t)\phi_k(r)dr. \tag{B.24}$$

Or in matrix form (since it holds for every k):

$$\underbrace{\begin{bmatrix} \int_a^R \phi_1(r)\phi_1(r)dr & \int_a^R \phi_1(r)\phi_2(r)dr & \cdots & \int_a^R \phi_1(r)\phi_N(r)dr \\ \int_a^R \phi_2(r)\phi_1(r)dr & \int_a^R \phi_2(r)\phi_2(r)dr & \cdots & \int_a^R \phi_2(r)\phi_N(r)dr \\ \vdots & \vdots & \ddots & \vdots \\ \int_a^R \phi_N(r)\phi_1(r)dr & \int_a^R \phi_N(r)\phi_2(r)dr & \cdots & \int_a^R \phi_N(r)\phi_N(r)dr \end{bmatrix}}_{G} \begin{bmatrix} \frac{dT_1(t)}{dt} + \lambda_1 T_1(t) \\ \frac{dT_2(t)}{dt} + \lambda_2 T_2(t) \\ \vdots \\ \frac{dT_N(t)}{dt} + \lambda_N T_N(t) \end{bmatrix} = \begin{bmatrix} \int_a^R H(r,t)\phi_1(r)dr \\ \int_a^R H(r,t)\phi_2(r)dr \\ \vdots \\ \int_a^R H(r,t)\phi_N(r)dr \end{bmatrix}. \tag{B.25}$$

Such that

$$\begin{bmatrix} \frac{dT_1(t)}{dt} + \lambda_1 T_1(t) \\ \frac{dT_2(t)}{dt} + \lambda_2 T_2(t) \\ \vdots \\ \frac{dT_N(t)}{dt} + \lambda_N T_N(t) \end{bmatrix} = G^{-1} \begin{bmatrix} \int_a^R H(r,t)\phi_1(r)dr \\ \int_a^R H(r,t)\phi_2(r)dr \\ \vdots \\ \int_a^R H(r,t)\phi_N(r)dr \end{bmatrix}. \tag{B.26}$$

So we have

$$\begin{aligned} &\frac{dT_n(t)}{dt} + \lambda_n T_n(t) = \sum_{j=1}^{N} \left[G^{-1}\right]_{n,j} \int_a^R H(r,t)\phi_j(r)dr \\ \implies & e^{\lambda_n t}\frac{dT_n(t)}{dt} + e^{\lambda_n t}\lambda_n T_n(t) = e^{\lambda_n t}\sum_{j=1}^{N} \left[G^{-1}\right]_{n,j} \int_a^R H(r,t)\phi_j(r)dr \\ \implies & \frac{d}{dt}\left[e^{\lambda_n t}T_n(t)\right] = e^{\lambda_n t}\sum_{j=1}^{N} \left[G^{-1}\right]_{n,j} \int_a^R H(r,t)\phi_j(r)dr \\ \implies & e^{\lambda_n t}T_n(t) - T_n(0) = \int_0^t e^{\lambda_n \bar{t}}\sum_{j=1}^{N} \left[G^{-1}\right]_{n,j} \int_a^R H(r,\bar{t})\phi_j(r)dr d\bar{t} \\ \implies & T_n(t) = e^{-\lambda_n t}T_n(0) + e^{-\lambda_n t}\int_0^t e^{\lambda_n \bar{t}}\sum_{j=1}^{N} \left[G^{-1}\right]_{n,j} \int_a^R H(r,\bar{t})\phi_j(r)dr d\bar{t}, \end{aligned} \tag{B.27}$$

where $T_n(0)$ is found similarly by multiplying equation B.21 at $t = 0$ by $\phi_k(r)$ and integrating from a to R to obtain

$$T_n(0) = \sum_{j=1}^{N} \left[G^{-1}\right]_{n,j} \int_a^R \left(h(r) - \psi(r,0)\right)\phi_j(r)\,\mathrm{d}r\,. \tag{B.28}$$

Writing this out using Fubini's theorem yields

$$\begin{aligned} T_n(t) =& e^{-\lambda_n t}\Bigg(\sum_{j=1}^{N} \left[G^{-1}\right]_{n,j} \int_a^R h(r)\phi_j(r)dr - \sum_{j=1}^{N} \left[G^{-1}\right]_{n,j} \int_a^R \frac{r-a}{R-a}\phi_j(r)dr \\ &- \frac{1}{\lambda_n}\sum_{j=1}^{N} \left[G^{-1}\right]_{n,j} \int_a^R \frac{1}{r}\left(\kappa - \frac{Q}{\pi D}\right)\frac{1}{R-a}\phi_j(r)dr\Bigg) \\ &- f(t)\sum_{j=1}^{N} \left[G^{-1}\right]_{n,j} \int_a^R \frac{R-r}{R-a}\phi_j(r)dr \\ &+ \int_0^t f(\bar{t})e^{\lambda_n(\bar{t}-t)}d\bar{t}\left(-\sum_{j=1}^{N} \left[G^{-1}\right]_{n,j} \int_a^R \frac{1}{r}\left(\kappa - \frac{Q}{\pi D}\right)\frac{1}{R-a}\phi_j(r)dr + \lambda_n \sum_{j=1}^{N} \left[G^{-1}\right]_{n,j} \int_a^R \frac{R-r}{R-a}\phi_j(r)dr\right) \\ &+ \frac{1}{\lambda_n}\sum_{j=1}^{N} \left[G^{-1}\right]_{n,j} \int_a^R \frac{1}{r}\left(\kappa - \frac{Q}{\pi D}\right)\frac{1}{R-a}\phi_j(r)dr, \end{aligned} \tag{B.29}$$

where we have used partial integration in this step to remove the time derivative $f'(t)$.

Appendix C

Numerical Scheme

In this chapter, a numerical method is described using first order estimates for s_x and s_r. The final results in Section 4.3 are obtained using second order forward estimates. That second order method can be described analogously.

We divide the x and r domains in n and m equidistant grid points respectively as shown in Figure C.1. The distances are $\Delta x = L/(n+1)$ and $\Delta r = (R-a)/(m+1)$. The salinity at the interface will be denoted by $\hat{s}$ and will later be eliminated from the equations by using the coupling conditions.

River

The PDE contains a first and second order spatial derivative. Since we wish to approximate the first derivative at the interface, we will use forward differences for the first derivative. From expanding $s(x+\Delta x)$ around x we find

$$s(x) = s(x), \tag{C.1}$$

$$s(x+\Delta x) = s(x) + \Delta x \left.\frac{\partial s}{\partial x}\right|_x + O(\Delta x)^2. \tag{C.2}$$

Subtracting C.1 from C.2 and dividing by Δx yields

$$\left.\frac{\partial s}{\partial x}\right|_x = \frac{s(x+\Delta x) - s(x)}{\Delta x} + O(\Delta x). \tag{C.3}$$

To approximate the second derivative we expand $s(x+\Delta x)$ and $s(x-\Delta x)$ around x:

$$s(x-\Delta x) = s(x) - \Delta x \left.\frac{\partial s}{\partial x}\right|_x + \frac{(\Delta x)^2}{2}\left.\frac{\partial^2 s}{\partial x^2}\right|_x - \frac{(\Delta x)^3}{6}\left.\frac{\partial^3 s}{\partial x^3}\right|_x + O(\Delta x)^4, \tag{C.4}$$

$$s(x) = s(x), \tag{C.5}$$

$$s(x+\Delta x) = s(x) + \Delta x \left.\frac{\partial s}{\partial x}\right|_x + \frac{(\Delta x)^2}{2}\left.\frac{\partial^2 s}{\partial x^2}\right|_x + \frac{(\Delta x)^3}{6}\left.\frac{\partial^3 s}{\partial x^3}\right|_x + O(\Delta x)^4. \tag{C.6}$$

Adding C.4 and C.6, subtracting C.5 twice and dividing by $(\Delta x)^2$ yields

$$\left.\frac{\partial^2 s}{\partial x^2}\right|_x = \frac{s(x-\Delta x) - 2s(x) + s(x+\Delta x)}{(\Delta x)^2} + O(\Delta x)^2. \tag{C.7}$$

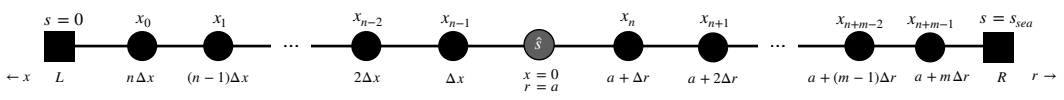

Figure C.1: The domains $0 < x < L$ and $a < r < R$ are discretised in n and m equidistant points. The boundary salinity at $x = 0$ is denoted $\hat{s}$ and will be eliminated from the numerical scheme.

Note that the time variable was left out of the notation as all values are at the same time. We now indicate $s_i = s(x_i)$ for x_i the equidistant grid points. Then the approximations of the derivatives are

$$\frac{\partial s_i}{\partial x} \approx \frac{s_{i-1} - s_i}{\Delta x}, \tag{C.8}$$

$$\frac{\partial^2 s_i}{\partial x^2} \approx \frac{s_{i-1} - 2s_i + s_{i+1}}{\Delta x}. \tag{C.9}$$

We pay special attention to the boundary cases $i = 0$ and $i = n - 1$:

$$\frac{\partial s_0}{\partial x} \approx \frac{0 - s_0}{\Delta x} \tag{C.10}$$

$$\frac{\partial^2 s_0}{\partial x^2} \approx \frac{0 - 2s_0 + s_1}{(\Delta x)^2} \tag{C.11}$$

$$\frac{\partial s_{n-1}}{\partial x} \approx \frac{s_{n-2} - s_{n-1}}{\Delta x} \tag{C.12}$$

$$\frac{\partial^2 s_{n-1}}{\partial x^2} \approx \frac{s_{n-2} - 2s_{n-1} + \hat{s}}{(\Delta x)^2} \tag{C.13}$$

Sea

In the sea we use forward differences to estimate the first derivative for the same reason.

$$\frac{\partial s_i}{\partial r} \approx \frac{s_{i+1} - s_i}{\Delta r} \tag{C.14}$$

$$\frac{\partial^2 s_i}{\partial r^2} \approx \frac{s_{i+1} - 2s_i + s_{i-1}}{\Delta r} \tag{C.15}$$

We pay special attention to the boundary cases $i = n$ and $i = n + m - 1$:

$$\frac{\partial s_n}{\partial r} \approx \frac{s_{n+1} - s_n}{\Delta r} \tag{C.16}$$

$$\frac{\partial^2 s_n}{\partial r^2} \approx \frac{\hat{s} - 2s_n + s_{n+1}}{(\Delta r)^2} \tag{C.17}$$

$$\frac{\partial s_{n+m-1}}{\partial r} \approx \frac{1 - s_{n+m-1}}{\Delta r} \tag{C.18}$$

$$\frac{\partial^2 s_{n+m-1}}{\partial r^2} \approx \frac{s_{n+m-2} - 2s_{n+m-1} + 1}{(\Delta r)^2} \tag{C.19}$$

Coupling

The first coupling conditions is already embedded into the scheme by $\hat{s}$. The second coupling condition was simplified to:

$$-ks_x(0) = \kappa s_r(a). \tag{C.20}$$

Approximating $s_x(0)$ and $s_r(a)$, we find

$$-k\frac{s_{n-1} - \hat{s}}{\Delta x} = \kappa\frac{s_n - \hat{s}}{\Delta r}, \tag{C.21}$$

which we write as

$$\hat{s} = \alpha s_n + \beta s_{n-1}, \tag{C.22}$$

with

$$\alpha = \frac{\kappa\Delta x}{k\Delta r + \kappa\Delta x}, \quad \beta = \frac{k\Delta r}{k\Delta r + \kappa\Delta x}.$$

Matrix Notation

Let us denote

$$\mathbf{s}^j = \begin{bmatrix} s_0(t_j) \\ \vdots \\ s_{n-1}(t_j) \\ s_n(t_j) \\ \vdots \\ s_{n+m-1}(t_j) \end{bmatrix}, \tag{C.23}$$

where t is now also discretised. We can then write

$$\frac{\partial \mathbf{s}^j}{\partial t} = K\mathbf{s}^j + \mathbf{b}, \tag{C.24}$$

where

$$K = \begin{bmatrix} \frac{-2k}{(\Delta x)^2} - \frac{Q/A}{\Delta x} & \frac{k}{(\Delta x)^2} & 0 & & & & & & & \\ \frac{k}{(\Delta x)^2} + \frac{Q/A}{\Delta x} & \frac{-2k}{(\Delta x)^2} - \frac{Q/A}{\Delta x} & \frac{k}{(\Delta x)^2} & \ddots & & & & & & \\ & \ddots & \ddots & \ddots & & & & & & \\ & & \frac{k}{(\Delta x)^2} + \frac{Q/A}{\Delta x} & \frac{-2k+k\beta}{(\Delta x)^2} - \frac{Q/A}{\Delta x} & \frac{k\alpha}{(\Delta x)^2} & 0 & & & & \\ & & 0 & \frac{\kappa\beta}{(\Delta r)^2} & \frac{-2\kappa+\kappa\alpha}{(\Delta r)^2} - \frac{\kappa - Q/\pi D}{\Delta r(\Delta r + a))} & \ddots & & & & \\ & & & & \ddots & \frac{\kappa}{(\Delta r)^2} + \frac{\kappa - Q/\pi D}{\Delta r(\Delta r + a))} & & & & \\ & & & & & \ddots & \ddots & & & \\ & & & & & \frac{\kappa}{(\Delta r)^2} & \frac{-2\kappa}{(\Delta r)^2} - \frac{\kappa - Q/\pi D}{\Delta r((m-1)\Delta r + a))} & \frac{\kappa}{(\Delta r)^2} + \frac{\kappa - Q/\pi D}{\Delta r((m-1)\Delta r + a))} & & \\ & & & & & 0 & \frac{\kappa}{(\Delta r)^2} & \frac{-2\kappa}{(\Delta r)^2} - \frac{\kappa - Q/\pi D}{\Delta r(m\Delta r + a))} & & \end{bmatrix},$$

and

$$\mathbf{b} = \begin{bmatrix} 0 \\ \vdots \\ 0 \\ 0 \\ \vdots \\ \frac{\kappa}{(\Delta r)^2} + \frac{\kappa - Q/\pi D}{\Delta r((m-1)\Delta r + a))} \end{bmatrix}. \tag{C.25}$$

We now use the trapezoidal rule or *Crank-Nicolson* method of time integration to calculate the solution at later time steps

$$\mathbf{s}^{j+1} = \mathbf{s}^j + \frac{\Delta t}{2}\left(K\mathbf{s}^j + \mathbf{b} + K\mathbf{s}^{j+1} + \mathbf{b}\right), \tag{C.26}$$

or in explicit form

$$\mathbf{s}^{j+1} = \left[I - \frac{\Delta t}{2}K\right]^{-1}\left[I + \frac{\Delta t}{2}K\right]\mathbf{s}^j + \Delta t\left[I - \frac{\Delta t}{2}K\right]^{-1}\mathbf{b}. \tag{C.27}$$

Calculating the inverse matrix is done numerically.

The trapezoidal method follows from expanding $s(t)$ and $s(t + \Delta t)$ around $t + \Delta t/2$, leaving out position x in notation for simplicity:

$$s(t + \Delta t/2) = s(t) + \frac{\Delta t}{2}\left.\frac{\partial s}{\partial t}\right|_t + O(\Delta t)^2, \tag{C.28}$$

$$s(t + \Delta t/2) = s(t + \Delta t) - \frac{\Delta t}{2}\left.\frac{\partial s}{\partial t}\right|_{t+\Delta t} + O(\Delta t)^2. \tag{C.29}$$

Equating C.28 and C.29 and rearranging terms yields

$$s(t + \Delta t) = s(t) + \frac{\Delta t}{2}\left(\left.\frac{\partial s}{\partial t}\right|_t + \left.\frac{\partial s}{\partial t}\right|_{t+\Delta t}\right), \tag{C.30}$$

which takes the form of C.26 when the time derivatives are expressed in spatial derivatives by the partial differential equation and then approximated as described before.

Appendix D

Accuracy and Convergence

The purpose of this chapter is to provide some background information and results that have lead to the choices of numerical parameters such as the number of eigenfunctions and time steps.

D.1 Eigenfunction Expansion

First we wish to check how well we can approximate the initial condition as a sum of eigenfunctions $\sum_{n=1}^{N} a_n \phi_n(x)$. Furthermore we want to see how well the solution converges to the final equilibrium solution. We now consider the river only problem with fixed boundary conditions. Figure D.1 shows the difference between the eigenfunction solution and the initial condition and equilibrium at $t = 0$ s and $t = 10^7$ s respectively for $N = 10, 20, 30, 50$ eigenfunctions. We observe that the use of the first 30 eigenfunctions is sufficiently accurate by this metric for the purpose of most calculations.

Figure D.2 shows a similar result for the sea only problem with fixed boundary conditions. The errors are of the same order and the use of the first 30 eigenfunctions is likely sufficient. However, as shown in Figure 4.8, the adjustment time calculations show oscillations. Everywhere except for near the boundary of the domain, these oscillations become smaller as more eigenfunctions are used. However, due to computational limitations caused by the expensive inverting of the matrix G, we cannot practically use much more than 100 eigenfunctions at best. To investigate whether the solution obtained by only 30 eigenfunctions is close to the actual solution, we also approximate it numerically. The result is shown in Figure D.3. The numerical solution is indeed similar to the eigenfunction solution but without oscillations. Further computations for example in Figure 4.10 are therefore still done with the quicker eigenfunction method.

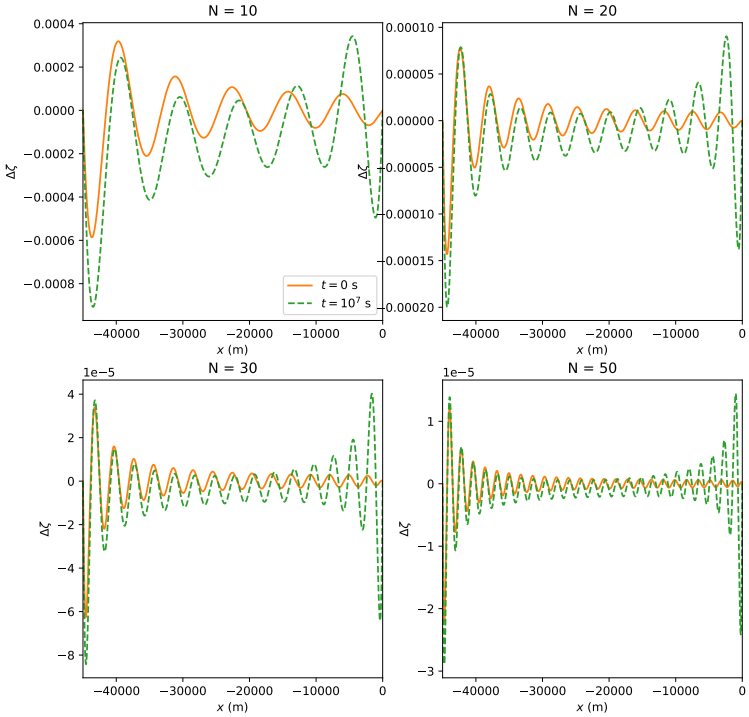

Figure D.1: For the river only problem with fixed boundary conditions, the difference between the initial condition and its approximation in eigenfunctions and the difference between the equilibrium solution and the approximation using eigenfunctions at $t = 10^7$ s are shown in solid orange and dashed green lines respectively for $N = 10, 20, 30, 50$ eigenfunctions. Note that the scales on the vertical axes differ. As more eigenfunctions are used, the error decreases.

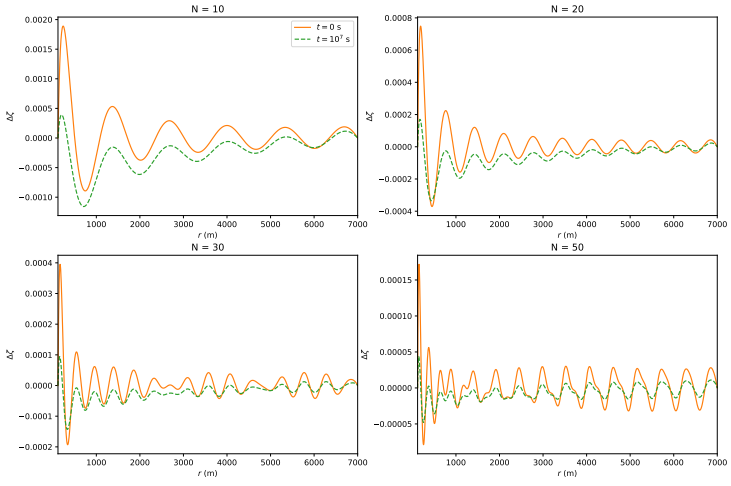

Figure D.2: For the sea only problem with fixed boundary conditions, the difference between the initial condition and its approximation in eigenfunctions and the difference between the equilibrium solution and the approximation using eigenfunctions at $t = 10^7$ s are shown in solid orange and dashed green lines respectively for $N = 10, 20, 30, 50$ eigenfunctions. Note that the scales on the vertical axes differ. As more eigenfunctions are used, the error decreases.

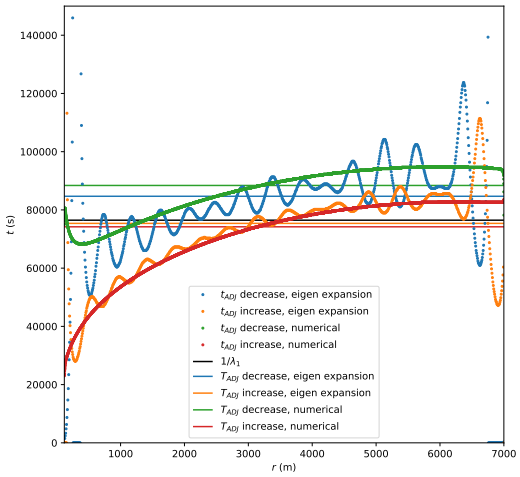

Figure D.3: For the sea only problem with fixed boundary conditions, the adjustments times t_{ADJ} and T_{ADJ} for increasing and decreasing salinity due to doubling and halving of freshwater discharge is shown. The calculations are done using 30 eigenfunctions (blue and orange) and using a first order finite difference scheme with $m = 6000$ spatial steps and $\Delta t = 200$ s (green and red). The results are similar.

D.2 Numerical Scheme

In this section we will briefly consider the effect of using the previously described numerical scheme with first or second order forward differences and choosing different spatial steps Δx and Δr and a different time step Δt. Figure D.4 shows the difference between the numerical solution at $t = 10^6$ s and the analytical equilibrium solution for different numerical parameters using the first order differences. The solution at $t = 10^7$ s is not noticeably different, such that we infer that equilibrium is (almost) reached. For all three different values of Δt, no difference is visible. Decreasing Δx and Δr does result in a much better result, as expected.

It was found by trial and error that it is more important that Δr is small than Δx, hence we have chosen to have more grid points in the sea than in the river. This is likely the result of this specific parameter set where $\kappa < k$ and the gradient and curvature are larger in the domain of the sea. The solid lines in figure D.5 show the error at $t = 10^7$ s for varying Δr and Δx and constant Δt. In dashed lines, the result is shown for the scheme with second order upwind differences. This scheme was also considered since it is of second order and could therefore possibly increase accuracy. Remember that a forward scheme is required at the coupling boundary. It appears that this second order scheme does indeed perform much better. The second order method takes more time because the K matrix has fewer zero entries, which particularly increases the time needed to invert the matrices.

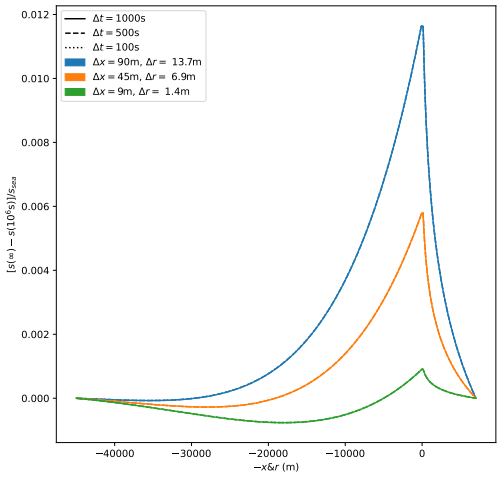

Figure D.4: The difference between the numerical solution at $t = 10^6$ s and the equilibrium solution of the coupled solution is shown for different numerical parameters. Step sizes smaller than 1000 s do not show any noticeable difference, while increasing spatial resolution does significantly lower the error.

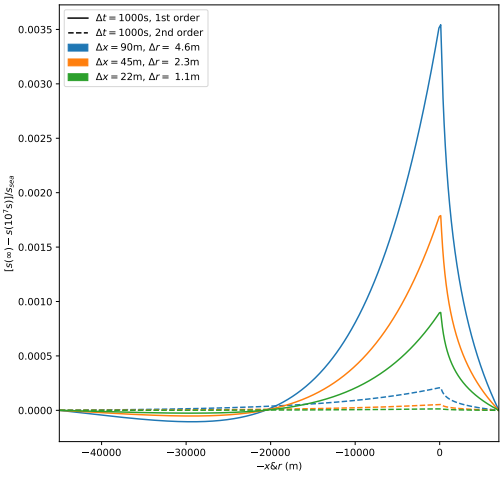

Figure D.5: The difference between the numerical solution at $t = 10^7$ s and the equilibrium solution of the coupled solution is shown for different numerical parameters and schemes. Δt is now fixed. Δx, Δr and the numerical scheme are varied. It appears that decreasing Δr and Δx improves the result. The second order upwind differences scheme has a much smaller error in all considered cases. Interestingly, the error is largest at the mouth of the river for each calculation.

Appendix E

Literature Comparison

In this chapter we briefly elaborate on some of the claims in the discussion. In particular we will demonstrate how the time scales found by C. Kranenburg (1986) and MacCready (2007) compare with our results.

Kranenburg 1986

Kranenburg uses a perturbation method on an estuary with varying cross section and a general dispersion. By studying the point where the difference between the salinity and steady state salinity is maximal, he finds a time scale t_s given by

$$t_s = \int_0^L A \left| \frac{\partial \tilde{s}}{\partial Q} \right| dx, \tag{E.1}$$

where $\tilde{s}$ is the quasi-steady solution depending on discharge Q. When we assume infinite intrusion length L, such that the boundary conditions as given by Kranenburg are satisfied, we have

$$\tilde{s}(x) = e^{-\frac{Q}{kA}x}. \tag{E.2}$$

One can then derive

$$t_s = \frac{k}{(Q/A)^2}. \tag{E.3}$$

For the same dispersion but with finite intrusion length, the time scale presented in our study is given by

$$\begin{aligned} t_{ADJ} &= \frac{1}{\lambda_1} \\ &= \frac{1}{\frac{(Q/A)^2}{4k} + k\left(\frac{\pi}{L}\right)^2}. \end{aligned} \tag{E.4}$$

As $L \to \infty$, the scaling becomes the same for $(Q/A)^2$ and k.

MacCready 2007

MacCready analytically developed a time scale via a very different approach. He assumes dispersion is dominated by a term proportional to either s_x or $(s_x)^3$. He linearises the equations to obtain an ODE for the intrusion length. In the tidal stirring dominated case with dispersion proportional to s_x, which is what we have modeled as well, he finds a time scale $t_{MC} = \frac{1}{2}L/u_0$ where L/u_0 is the time it takes for a particle to flow through the entire estuary.

The result of figure 4.4 warrants further investigation since $\frac{1}{2}L/u_0 \approx 3.4 \cdot 10^5$ s, which is reasonably close to the result observed of above $2.5 \cdot 10^5$ s near the intrusion length, that may be distorted due to convergence of the eigenfunctions. Figure E.1 shows a similar result in dimensionless parameters for variable Péclet number. The time scale of MacCready is made dimensionless by dividing by the dispersion time $\tau_{MC} = \frac{k}{L^2}t_{MC} = \frac{1}{2\mathrm{Pe}}$ and shown in the figure. It appears than the local adjustment time τ_{ADJ} is not close to τ_{MC} in general. This is not a surprise when we

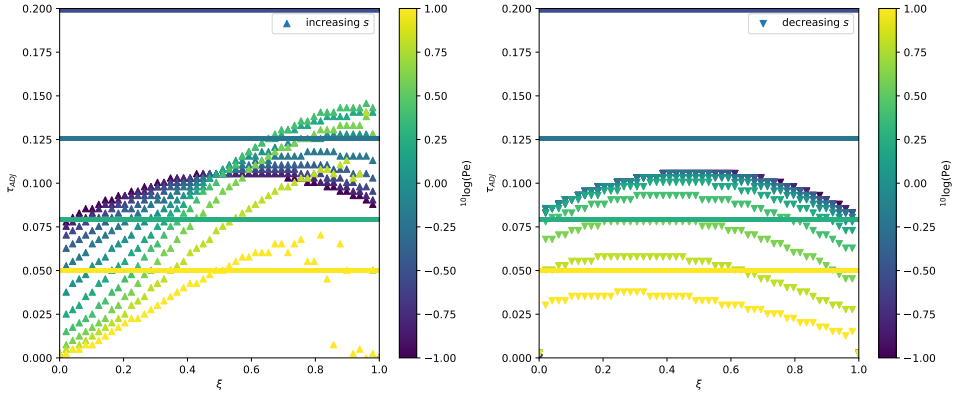

Figure E.1: The local dimensionless adjustment time τ_{ADJ} is shown as function of position ξ for different Péclet numbers. The left pane shows results for increasing salinity due to halving of Pe and the right pane shows results for decreasing salinity due to halving of Pe. The intrusion length time scale τ_{MC} from MacCready (2007) is shown as horizontal line. The result is obtained using 30 eigenfunctions.

compare the assumptions in both methods. MacCready estimates salinity to decrease linearly from the ocean salinity at the mouth of the estuary to 0 at the intrusion length, which corresponds to small Péclet numbers. Our model may have a significant non realistic loss of salt through the up estuary boundary resulting in underestimation of τ_{ADJ}

This result also shows that the positional variation in τ_{ADJ} depends on the Péclet number. For larger Pe the distribution more resembles a straight line intersecting $\tau = 0$ at $\xi = 0$ for increasing salinity since salt enters from the mouth at $\xi = 0$ and intersecting $\tau = 0$ at $\xi = 1$ for decreasing salinity since then salt is first flushed away from near the intrusion length.